Physical study of the non-equilibrium development of a turbulent thermal boundary layer

Matteo Gelain, O. Gicquel, A Couilleaux, R. Vicquelin

Physical study of the non-equilibrium development of a turbulent thermal boundary layer

M. Gelain[1,2]†, O. Gicquel[1], A. Couilleaux[2] and R. Vicquelin[1]‡

[1]Laboratoire EM2C, CNRS, CentraleSupélec, Université Paris-Saclay, Gif-sur-Yvette, France
[2]Safran Aircraft Engines, Rond-point René Ravaud, 77550 Moissy-Cramayel, France

(Received xx; revised xx; accepted xx)

The direct numerical simulation of a non-equilibrium turbulent heat transfer case is performed in a channel flow, where non-equilibrium is induced by a step change in surface temperature. The domain is thus made of two parts in the streamwise direction. Upstream, the flow is turbulent, homogeneous in temperature and the channel walls are adiabatic. The inflow conditions are extracted from a recycling plane located further downstream so that a fully developed turbulent adiabatic flow reaches the second part. In the domain located downstream, isothermal boundary conditions are prescribed at the walls. The boundary layer, initially at equilibrium, is perturbed by the abrupt change of boundary conditions and a non-equilibrium transient phase is observed until, further downstream, the flow reaches a new equilibrium state presenting a fully developed thermal boundary layer. The study focuses on the spatial transient phase, identifies the main non-equilibrium effects and contrasts these results with usual assumptions of equilibrium turbulent heat transfer. Mean and root-mean-square profiles of temperature and velocity, as well as the respective energy and momentum balances, are presented and discussed along with budgets of second-order moment balance equations for the enthalpy variance and the wall-normal heat flux. For several quantities, an equilibrium near-wall region is identified even near the leading edge while the boundary layer is still developing. Finally, the evolution of the turbulent Prandtl number along the channel flow is investigated and shows that it reaches equilibrium only further downstream.

1. Introduction

Turbulent heat transfer is encountered in numerous industrial applications and in most cases the turbulent heat exchange takes place in non-equilibrium flows. It is the case, for instance, of the surface air-oil heat exchangers implemented in modern aircraft engines by-pass ducts, where an essentially temperature-homogeneous flow makes contact with a heated surface and is therefore abruptly subjected to a temperature gradient.

Yet, it is the interest in the behaviour of the atmospheric boundary layer which drew first attention to turbulent heat transfer in non-equilibrium flows, both theoretically and experimentally (see Antonia *et al.* 1977). The case where non-equilibrium is induced by a step change in surface temperature is the simplest example of non-equilibrium turbulent heat transfer and literature is abundant on the matter. Spalding (1961) derived a mathematically exact solution for a developing thermal boundary layer while assuming the motion of the flow to be perfectly described by the law of the wall. Experimentally,

† Email address for correspondence: matteo.gelain@safrangroup.com
‡ Email address for correspondence: ronan.vicquelin@centralesupelec.com

Johnson & Whippany (1957) studied the development of a thermal boundary layer on a smooth flat plate and presented mean temperature and velocity profiles while focusing on fluctuating profiles in a later work (Johnson *et al.* 1959). Blom (1970) carried out a similar study, comparing mean temperature profiles to the theoretical predictions of Spalding (1961) and presenting the evolution of the turbulent Prandtl number. Similar experimental works can be found in Fulachier (1972), Hoffmann & Perry (1979), Ng *et al.* (1982), Taylor *et al.* (1990) and, more recently, Biles *et al.* (2019) while Antonia *et al.* (1977) and Teitel & Antonia (1993) studied the case of a step change in wall heat flux in a flat plate and turbulent channel flow configuration, respectively.

In spite of its Reynolds number limitation, direct numerical simulation (DNS) is undoubtedly the most accurate tool available for the investigation of turbulent heat transfer since all the turbulent scales are solved and no modelling is needed. The first DNS addressing turbulent heat transfer is that of Kim & Moin (1989), where the transport of three passive scalars at different molecular Prandtl numbers is considered in a fully developed channel flow at a friction Reynolds number of $\mathrm{Re}_\tau = 180$. Several works followed, aiming at understanding the influence on the flow statistics of the Reynolds number and molecular Prandtl number (e.g. Papavassiliou & Hanratty 1997; Kawamura *et al.* 1999; Abe *et al.* 2001) as well as of the isothermal or iso-flux boundary conditions (e.g. Kasagi *et al.* 1992; Kawamura *et al.* 2000). Li *et al.* (2009) and Wu & Moin (2010), instead, are examples of DNS with passive scalar performed in a flat plate configuration. Other authors focused on the coupling between turbulence and temperature gradient, analysis which is possible only if temperature is not handled as a passive scalar. Most of these DNS were performed in supersonic channel flows (see Coleman *et al.* 1995; Huang *et al.* 1995; Morinishi *et al.* 2004; Tamano & Morinishi 2006) while only a few focused on low speed flows with high temperature gradients (see Nicoud 1999; Toutant & Bataille 2013).

All the numerical works mentioned so far represent cases of equilibrium flows and are undoubtedly the reference for understanding turbulent heat transfer in all its aspects (flow statistics, turbulent Prandtl number, wall scaling and much more). Nevertheless, questions arise concerning the validity of these findings in non-equilibrium configurations. Once more, DNS can be a powerful tool for the analysis of such flows yet literature is extremely less abundant on the matter. Seki & Kawamura (2005) performed the DNS of a fully developed channel flow with temperature as a passive scalar where the wall temperature is constant everywhere but in a small fraction of the bottom wall where it evolves along the streamwise direction attaining a peak. The step change of wall temperature significantly perturbs the mean and fluctuating temperature as well as turbulent Prandtl number. Hattori *et al.* (2007), Hattori *et al.* (2012) and Hattori *et al.* (2013) performed several DNS of non-equilibrium thermal boundary layers in the flat plate configuration. Hattori *et al.* (2007) analysed the effects of buoyancy on mean and fluctuating properties as well as on the turbulent budgets for a turbulent boundary layer at equilibrium facing a step change in wall temperature; temperature is treated as a passive scalar and buoyancy is thus introduced through a specific term added to the momentum equation. In Hattori *et al.* (2012), non-equilibrium is induced through the sudden vanishing of wall-heat flux and, in one of the two cases presented, with the addition of a forward facing step; temperature is also in this case a passive scalar. Similar analyses are carried out in Hattori *et al.* (2013), yet temperature, in this case, is not handled as a passive scalar and comparisons with large-eddy simulations (LES) and Reynolds-averaged Navier-Stokes equation simulations (RANS) are given.

LES is certainly another valid tool for studying non-equilibrium turbulent heat transfer yet, despite the large turbulent scales being solved, a certain degree of modelling is

needed for the smaller scales. Sanchez *et al.* (2014) and Bellec *et al.* (2017) performed the LES of a temperature-homogeneous fully developed channel flow making contact with anisothermal walls for $\mathrm{Re}_\tau = 180$ and $\mathrm{Re}_\tau = 395$, respectively. They showed the evolution of the mean and fluctuating temperature profiles as well as the impact of the step change in temperature on the mean and fluctuating velocity components.

The objective of this paper is to deepen the knowledge of turbulent non-equilibrium heat transfer which, as the literature review shows, has been investigated in a limited number of studies, especially in the case of flows with temperature-dependent properties. The intention is not only to describe and characterise a non-equilibrium flow, but also its gradual evolution towards a new equilibrium state.

To achieve the scope of the study, we perform the direct numerical simulation of a channel flow where a turbulent, fully developed, temperature-homogeneous flow at $\mathrm{Re}_\tau = 395$ makes contact with an isothermal wall; the step change in surface temperature leads to the development of a thermal layer, and, since temperature is not a passive scalar, the velocity boundary layer is also perturbed; the length of the isothermal wall allows the boundary layer to reach a new equilibrium state characterised by a fully developed thermal boundary layer. The study aims at accurately describing the evolution of the thermal layer with a particular focus on the non-equilibrium effects which can be identified. The analysis allows for defining a near-wall region where several quantities are equilibrated while understanding why others are not.

The work is organised as follows. In section §2, the problem is described in detail; the governing equations are presented as well as details about the study configuration are given. In section §3, the numerical set-up is validated with respect to reference results found in literature for equilibrium flows. In section §4, the results are presented: the impact of the isothermal wall on the velocity field is shown and the mean momentum equation is analysed in section §4.2; then, the evolution of the mean temperature profile and of the energy budgets is described in §4.3; the same is done in §4.4 for the fluctuating temperature and the wall-normal turbulent heat-flux along with the respective turbulent budgets; finally, the evolution of the turbulent Prandtl number along the channel flow is presented in section §4.5.

2. Problem description

In this section, details about governing equations and numerical scheme (§2.1), geometry, mesh and boundary conditions (§2.2) as well as initialisation (§2.3) are given.

2.1. *Governing equations and numerical scheme*

The full compressible Navier-Stokes equations are solved in the fluid without any turbulence model. The set of equations is the following:

$$\frac{\partial \rho}{\partial t} + \frac{\partial \rho u_i}{\partial x_i} = 0 \ , \tag{2.1}$$

$$\frac{\partial \rho u_i}{\partial t} + \frac{\partial \rho u_i u_j}{\partial x_j} = -\frac{\partial p}{\partial x_i} + \frac{\partial \boldsymbol{\tau}_{ij}}{\partial x_j} \ , \tag{2.2}$$

$$\frac{\partial \rho h}{\partial t} + \frac{\partial \rho u_j h}{\partial x_j} = \frac{\mathrm{D}p}{\mathrm{D}t} - \frac{\partial q_j^{cd}}{\partial x_j} + \boldsymbol{\tau}_{ij}\frac{\partial u_i}{\partial x_j} + S_{ener} \ , \tag{2.3}$$

where ρ, u_i, p, h are respectively the mass density, velocity components, static pressure and enthalpy per mass unit of the fluid; the fluid is considered to be an ideal gas with

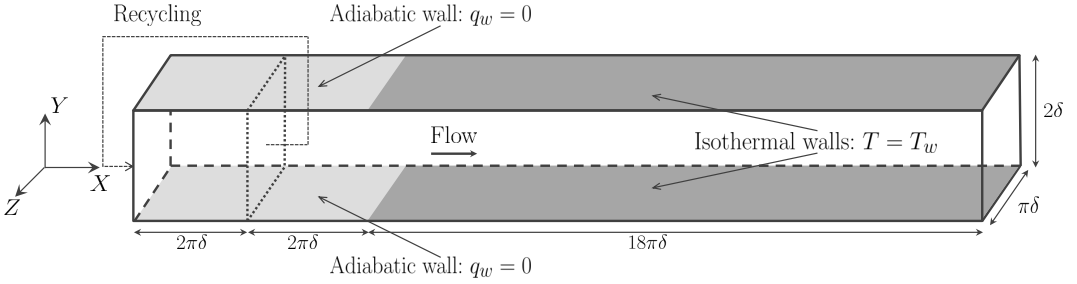

Figure 1: Computational domain of the present study.

temperature-tabulated thermodynamic coefficients, with the following equation relating pressure, density and temperature:

$$p = \rho r T, \tag{2.4}$$

where $r = 288.18$ J/(kg.K) is the mass-specific gas constant and T the fluid static temperature; gravity is neglected and not included in momentum equation (2.2); the viscous stress tensor $\boldsymbol{\tau}_{ij}$ is:

$$\boldsymbol{\tau}_{ij} = \mu \left(\frac{\partial u_i}{\partial x_j} + \frac{\partial u_j}{\partial x_i} \right) - \frac{2}{3} \mu \left(\frac{\partial u_k}{\partial x_k} \right) \delta_{ij} \tag{2.5}$$

where μ is the dynamic viscosity, computed via the Sutherland law and thus temperature-dependent:

$$\mu = \mu_{ref} \left(\frac{T}{T_{ref}} \right)^{\frac{3}{2}} \frac{T_{ref} + S_{suth}}{T + S_{suth}} , \tag{2.6}$$

with $\mu_{ref} = 1.716 \times 10^{-5}$ Pa.s, $T_{ref} = 273.15$ K and $S_{suth} = 110.6$ K; the conductive heat flux q_i^{cd}, following Fourier's law, is:

$$q_i^{cd} = -\lambda \frac{\partial T}{\partial x_i} , \tag{2.7}$$

where λ is the fluid conductivity computed with the Prandtl number $\mathrm{Pr} = 0.71$; finally, S_{ener} is a source term added to the energy equation (2.3) whose role will be clarified in section §2.2.

The set of equations is solved by the parallel code AVBP (Schonfeld & Rudgyard 1999; Moureau *et al.* 2005) using a time-explicit finite-element two-step Taylor-Galerkin scheme (Colin & Rudgyard 2000) which provides third-order accuracy in space and time.

2.2. *Geometry, mesh and boundary conditions*

The geometry of the configuration studied is shown in figure 1. The computational domain is a channel flow of size $22\pi\delta \times 2\delta \times \pi\delta$ (where $\delta = 0.002$ m) which is made of two parts in the streamwise direction.

The upstream part has size $4\pi\delta \times 2\delta \times \pi\delta$, the upper and lower walls (with respect to the Y direction) are adiabatic and a no-slip boundary condition is prescribed, while periodic boundary conditions are applied in the spanwise direction Z. Differently from what happens in bi-periodic channel flows, in this case the flow is driven by a streamwise pressure gradient compensating the head losses generated along the whole domain shown in figure 1. As a consequence, no source terms are needed in the momentum equation.

The mesh is made of 420, 179 and 200 points in the streamwise, wall-normal and spanwise directions, respectively. In the Z direction the mesh is uniform; in the wall-normal

Size	$n_X \times n_Y \times n_z$	ΔX^+	ΔY^+	ΔZ^+	Re_τ	M	T_b (K)
$[4\pi\delta, 2\delta, \pi\delta]$	$420 \times 179 \times 200$	$[1.0 - 12.0]$	$[0.75 - 7.0]$	6.2	395	0.16	304.5

Table 1: Size, mesh, resolution and regime conditions of upstream (adiabatic) subdomain: n_X, n_Y and n_Z are the number of points in the X, Y and Z direction, ΔX^+, ΔY^+ and ΔZ^+ are the spatial resolutions in the three directions expressed in wall units, Re_τ is the friction Reynolds number, M the average Mach number and T_b the bulk temperature.

direction the mesh size, expressed in wall units, varies from $\Delta Y^+ = 0.75$ at the upper and lower walls to $\Delta Y^+ = 7$ at the centre of the channel; along the streamwise direction, the mesh size varies from $\Delta X^+ = 12$ at the inlet to $\Delta X^+ = 1$ at the interface with the downstream part of the channel flow.

The role of this part of the domain is to generate a temperature-homogeneous boundary layer at equilibrium with the regime conditions specified in table 1. In order to do so at a moderate cost, a recycling strategy is used: the three velocity components and the temperature imposed at the domain inlet via the Navier-Stokes Characteristic Boundary Condition (NSCBC) formalism (Poinsot & Veynante 2005; Moureau *et al.* 2005) are extracted from a recycling plane situated downstream at a distance of $2\pi\delta$.

Despite the low Mach number (see table 1), compressibility effects, which are fully considered in (2.1), (2.2) and (2.3), impact the recycling procedure. Similarly to a subsonic Fanno flow (see Ockendon *et al.* 2001), if inlet conditions were recycled without any sort of correction, the presence of wall friction would make the flow accelerate and the temperature diminish until the sonic condition is attained.

It is thus necessary to normalise the values extracted at the recycling plane with respect to a target average temperature $\langle T \rangle_{target}$ and streamwise velocity $\langle U \rangle_{target}$ which allow to obtain the regime specified in table 1. For every time iteration one has:

$$u_i(x, y, z, t)|_{x=0} = u_i(x, y, z, t)|_{x=2\pi\delta} \frac{\langle U \rangle_{target}}{\langle U \rangle_{x=2\pi\delta}} \ , \tag{2.8}$$

as well as,

$$T(x, y, z, t)|_{x=0} = T(x, y, z, t)|_{x=2\pi\delta} \frac{\langle T \rangle_{target}}{\langle T \rangle_{x=2\pi\delta}} \ , \tag{2.9}$$

where $\langle U \rangle_{x=2\pi\delta}$ is the average streamwise velocity and $\langle T \rangle_{x=2\pi\delta}$ the average temperature at the recycling plane at instant t. Given the low Mach number and the short distance between the inlet and the recycling plane, the correction applied to the temperature and the velocity components is minimal,

$$\left(1 - \langle U \rangle_{target} / \langle U \rangle_{x=2\pi\delta}\right) \sim 10^{-7},$$

$$\left(1 - \langle T \rangle_{target} / \langle T \rangle_{x=2\pi\delta}\right) \sim -10^{-7},$$

and yet necessary. Without, the bulk velocity drifts away and eventually diverges.

The downstream part of the domain has size $[18\pi\delta, 2\delta, \pi\delta]$, the upper and lower walls are isothermal, both at temperature $T_w = 400$ K, and a no-slip boundary condition is prescribed, while, analogously to the upstream part, the domain is periodic in the

spanwise direction. At the outlet, pressure is imposed via the NSCBC formalism and thus a streamwise pressure gradient driving the flow generates between the inlet and the exit of the domain.

The mesh has 1771, 179 and 200 points in the streamwise, wall-normal and spanwise direction, respectively. The mesh has the same point distribution of the upstream sub-domain along the Y and Z directions, while the mesh size varies from $\Delta X^+ = 1$ at the adiabatic-isothermal interface to $\Delta X^+ = 12$ at the outlet where wall units are still referred to the adiabatic conditions of the upstream sub-domain. This refinement along the streamwise direction allows to well capture the very first development region of the thermal boundary layer at the leading edge of the isothermal wall, where streamwise gradients can be important.

The role of the downstream part is to allow the thermal boundary layer to be fully developed and to attain a new equilibrium state before the exit. The fully developed regime is characterized by a scaled mean temperature profile which is homogeneous in the streamwise direction. The profile is scaled from the possibly varying bulk and wall temperatures in a general case. Without any source term in the energy equation, the mean temperature and its bulk value approach asymptotically the fixed wall temperature in the present case. In order to appreciate more clearly the fully developed regime, a source term is added to the energy equation (2.3) to yield a homogeneous mean temperature that results from the balance between the prescribed source term and the wall heat fluxes of the established flow $\overline{q_w}^{eq}$:

$$\overline{q_w}^{eq} \approx -S_{ener}\delta \ . \tag{2.10}$$

The source term S_{ener} is constant in time while being homogeneous in each subdomain in the following manner:

$$S_{ener}(x) = \begin{cases} 0 & for\ x \in [0, 4\pi\delta] \\ \\ \overline{S_{ener}}^{eq-isot} & for\ x \in [4\pi\delta, 22\pi\delta], \end{cases} \tag{2.11}$$

where $\overline{S_{ener}}^{eq-isot}$ is the time-averaged energy source term at equilibrium of the configuration described in section §3.2.

Since temperature is not a passive scalar in (2.3), the temperature gradient between the wall and the centre of the channel has an impact on the velocity boundary layer and on the momentum balance. This effect can be quantified (see Nicoud 1999), by the heat flux parameter $\mathrm{B}_q = q_w / \left(\rho_w c_{p_w} u_\tau T_w\right)$ where q_w is the wall heat flux, ρ_w and c_{p_w} respectively the mass density and the constant-pressure specific heat at the wall and u_τ the friction velocity defined as $u_\tau = \sqrt{\tau_w/\rho_w}$ where τ_w is the wall shear stress. Alternatively, one can compute the value of the heat flux parameter at equilibrium B_q^{eq} as a function of the source term added:

$$\mathrm{B}_q^{eq} = -\frac{S_{ener}\delta}{\rho_w c_{p_w} u_\tau T_w} \tag{2.12}$$

Table 2 summarises the size and the mesh resolution while table 3 details the regime conditions of the downstream part of the domain. Since the value of B_q^{eq} is of the order of 10^{-2} and the temperature ratio $\left(T_w/\overline{T}_c\right)^{out}$ is close to one, the impact of the temperature gradient on the momentum balance (see Wardana *et al.* 1994; Eames & Hunt 1997) is expected to be negligible, at least at equilibrium, as shown in section §3.2.

Size	$n_X \times n_Y \times n_z$	ΔX^+	ΔY^+	ΔZ^+
$[18\pi\delta, 2\delta, \pi\delta]$	$1771 \times 179 \times 200$	$[1.0 - 12.0]$	$[0.75 - 7.0]$	6.2

Table 2: Size, mesh and spatial resolution of downstream (isothermal) sub-domain.

T_w (K)	B_q^{eq}	$(\mathrm{Nu})^{out}$	$(\mathrm{Re}_\tau)^{out}$	$\left(\frac{T_w}{\overline{T}_c}\right)^{out}$	$\frac{T_w}{\overline{T}_{in}}$
400	0.017	27.4	292	1.36	1.31

Table 3: Regime conditions of downstream (isothermal) sub-domain: $(\mathrm{Nu})^{out} = \left(2\delta\frac{q_w}{\lambda_w(T_w - T_c)}\right)^{out}$ is the Nusselt number, $(\mathrm{Re}_\tau)^{out}$ the friction Reynolds number and $\left(T_w/\overline{T}_c\right)^{out}$ the temperature ratio between the wall and the centre of the channel, all three evaluated at the outlet; $T_w/\overline{T}_{in}$ is the temperature ratio between the wall and the inlet.

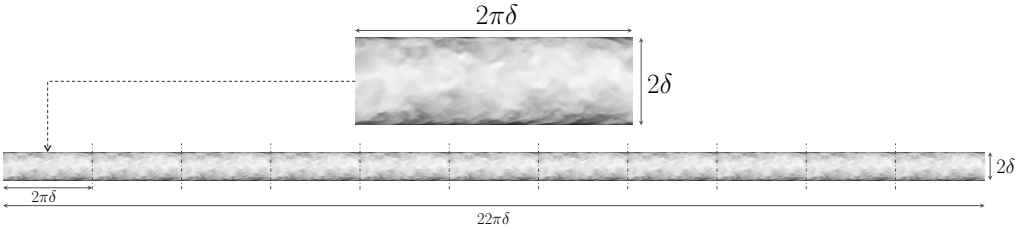

Figure 2: Schematic representation of the initial solution. The conservative fields (in this case ρu) of a $2\pi\delta \times 2\delta \times \pi\delta$ adiabatic channel flow at equilibrium is repeated periodically in the streamwise direction eleven times.

2.3. *Initialisation and computing time*

In order to minimise the transient period necessary for the flow to reach the statistically steady state, the initial conservative fields are extracted from a smaller bi-periodic adiabatic channel flow at equilibrium, of which details are given in section §3.1. The size of this channel flow being $[2\pi\delta, 2\delta, \pi\delta]$, the same solution is put in sequence eleven times in the streamwise direction to cover the whole length of $22\pi\delta$, as shown in figure 2. In this manner not only is the initial solution periodic along the Z axis but also between the inlet and the recycling plane.

The velocity boundary layer is then already fully developed at the start of the simulation but in order for the thermal boundary layer to develop and attain steady state, the initial solution is integrated during a transient time $\tau_{trans} = 18\pi\delta/\overline{u}$, *i.e.*, the time the average flow needs to cross the whole downstream part of the domain. Once the steady state is reached, flow statistics are collected over the duration $56\delta/u_\tau$, with u_τ the friction velocity computed at the outlet.

Size	$n_X \times n_Y \times n_z$	ΔX^+	ΔY^+	ΔZ^+
$[2\pi\delta, 2\delta, \pi\delta]$	$200 \times 179 \times 200$	12.4 (8.88)	$[0.75 - 7.0]$ ($[0.54 - 5]$)	6.2 (4.44)

Table 4: Size, mesh and spatial resolution (in parentheses for the case with isothermal walls) of the channel flow used for validation.

3. Equilibrium states and validation

This study is characterised by two distinct equilibrium states between which the flow evolves along the streamwise direction. The former is an adiabatic, fully developed turbulent flow in the upstream part of the domain; the latter is a fully developed turbulent thermal boundary layer at the outlet.
So as to analyse these equilibrium states, two distinct simulations are performed in the same regime conditions specified in tables 1 and 3 in a smaller bi-periodic channel flow of which size and mesh information is summarised in table 4. The mesh distribution is the same as in tables 1 and 2 in the wall-normal and spanwise direction while in the X direction the point distribution is in this case uniform since there are no streamwise singularities.

These computations are used to both validate the numerical set-up introduced in section §2 and as reference solutions for the aforementioned equilibrium states in section §4. Furthermore, as explained in section §2.3, the adiabatic bi-periodic channel flow is also used for initialisation.
In the following sections details about these simulations as well as the main results compared to literature are given. In the following, $\overline{(\cdot)}$ and $\widetilde{(\cdot)}$ denote Reynolds and Favre averages while $(\cdot)'$ and $(\cdot)''$ denote their respective fluctuating parts.

3.1. *Adiabatic bi-periodic channel flow*

The regime conditions of the flow are those specified in table 1. Since the channel flow is periodic in the streamwise direction, differently from the configuration of figure 1, a source term S_{M_x} is needed in the momentum equation in the streamwise direction in order to attain (and maintain) the specified friction Reynolds number. An energy source term S_{ener} is also applied to the energy equation, in order to prevent the flow from progressively heating up because of viscous effects and of the influence of S_{M_x}.
The two source terms dynamically control the bulk Reynolds number Re_b and the bulk enthalpy h_b of the channel flow acting like a PI controller as described in Zhang & Vicquelin (2016). The new set of equations is then the following:

$$\frac{\partial \rho}{\partial t} + \frac{\partial \rho u_i}{\partial x_i} = 0 \ , \tag{3.1}$$

$$\frac{\partial \rho u_i}{\partial t} + \frac{\partial \rho u_i u_j}{\partial x_j} = -\frac{\partial p}{\partial x_i} + \frac{\partial \boldsymbol{\tau}_{ij}}{\partial x_j} + S_{M_x}\delta_{1i} \ , \tag{3.2}$$

$$\frac{\partial \rho h}{\partial t} + \frac{\partial \rho u_j h}{\partial x_j} = \frac{\mathrm{D}p}{\mathrm{D}t} - \frac{\partial q_j^{cd}}{\partial x_j} + \boldsymbol{\tau}_{ij}\frac{\partial u_i}{\partial x_j} + u_i S_{M_x}\delta_{1i} + S_{ener} \ , \tag{3.3}$$

where, in this case, $\delta_{i,j}$ represents the Kronecker delta. For the two source terms one only has to specify the target value for the bulk Reynolds number and bulk enthalpy as well as the temporal constant of the PI controller, after which the two time-dependent source

Re_b	h_b (kJ)	$\alpha\delta/u_\tau$	$S_{M_x}\|_{t\to\infty}$	$S_{ener}\|_{t\to\infty}$
7062	307	1/3	$\overline{\tau_w}/\delta$	$-\overline{u}\frac{\overline{\tau_w}}{\delta}$

Table 5: Re_b and h_b are the target values for the bulk Reynolds number and enthalpy; α is the temporal constant of the PI controller expressed here in non-dimensional form with respect to the channel flow characteristic time δ/u_τ; $S_{M_x}|_{t\to\infty}$ and $S_{ener}|_{t\to\infty}$ are the asymptotic values for the two source terms once the target values are reached.

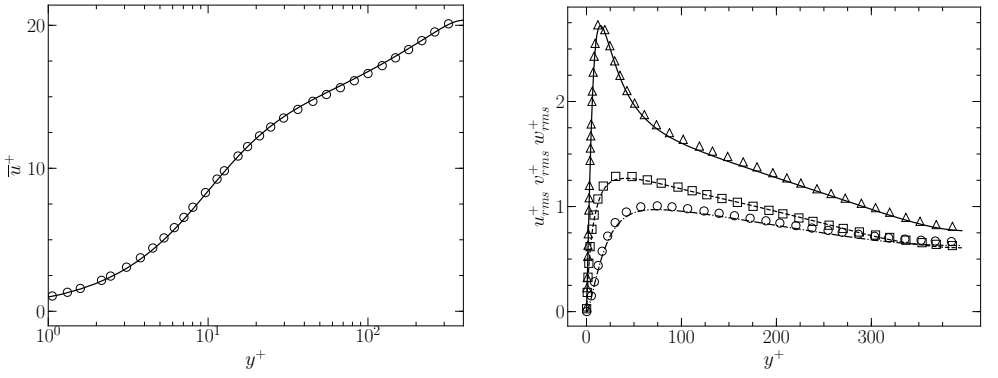

Figure 3: Mean profile of streamwise velocity (a): —— present results; ○ results from Kawamura *et al.* (1999). Profiles of r.m.s. streamwise, wall-normal and spanwise velocity respectively (b): ——, – · – · – and - - - - present results; △, ○ and □ results from Kawamura *et al.* (1999).

terms adapt automatically until the targets are reached. All these values are summarised in table 5.

Figure 3 shows the mean streamwise velocity profile $\overline{u}^+$ and the three root-mean-square (r.m.s.) velocity profiles adimensionalised with respect to the friction velocity $u_\tau = \sqrt{\tau_w/\nu_w}$ (where τ_w is the wall shear stress and ν_w is the kinematic viscosity at the wall) as a function of the wall distance expressed in wall units $y^+ = yu_\tau/\nu_w$. Results are compared to those of Kawamura *et al.* (1999) and a very good agreement is obtained for all the profiles.

3.2. *Bi-periodic channel flow with isothermal walls*

The regime conditions are those specified in table 3 while geometry and mesh are the same described in section §3.1. Also in this case, two source terms are added to the Navier-Stokes equations in order to attain the regime specified. Target bulk values as well as the asymptotic behaviour of the source terms are summarised in table 6, where $S_{ener}|_{t\to\infty}$ is the energy source term of (2.11) prescribed to the downstream part of the domain of figure 1.

Figure 4 shows the mean streamwise velocity and the three r.m.s. velocity profiles compared to those of Kawamura *et al.* (1999) obtained for an incompressible flow and the temperature treated as a passive scalar. In this case, two different wall scalings are used. The first, denoted as $(\cdot)^+$, is the classic wall scaling adopted in section §3.1; the second, denoted as $(\cdot)^*$ is the semi-local scaling (see Huang *et al.* 1995; Patel *et al.* 2015)

Re_b	h_b (kJ)	$\alpha\delta/u_\tau$	$S_{M_x}\|_{t\to\infty}$	$S_{ener}\|_{t\to\infty}$
7062	307	1/3	$\overline{\tau_w}/\delta$	$\frac{\overline{q_w}}{\delta} - \overline{u}\frac{\overline{\tau_w}}{\delta}$

Table 6: Target values for bulk Reynolds number and enthalpy; temporal constant of the PI controller; asymptotic values for the two source terms once the target values are reached, where $\overline{q_w}$ is the time-averaged wall heat flux.

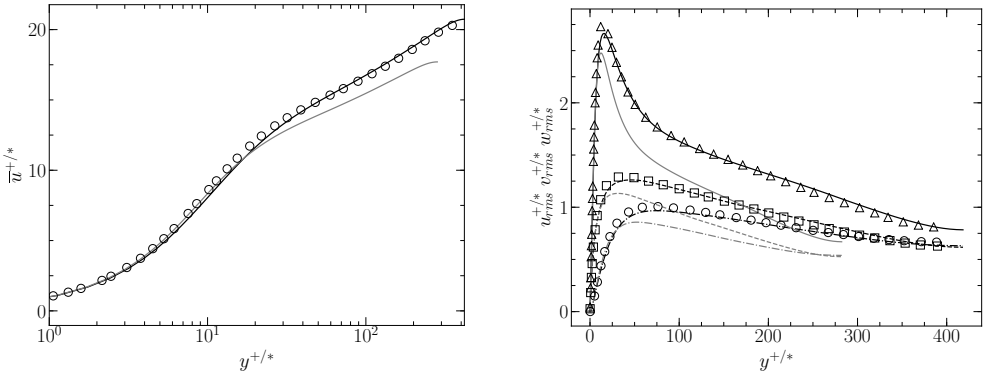

Figure 4: Mean profile of streamwise velocity (a): —— present results in classic (gray) and semi-local (black) scaling; ○ results from Kawamura *et al.* (1999).
Profiles of r.m.s. streamwise, wall-normal and spanwise velocity respectively (b): ——, – · – · – and - - - - present results in classic (gray) and semi-local (black) scaling; △, ○ and □ results from Kawamura *et al.* (1999).

using local fluid properties ρ, ν and c_p, where c_p is the thermal capacity at constant pressure, for the definition of the friction velocity $u_\tau = \sqrt{\tau_w/\rho}$, friction temperature $T_\tau = q_w/(\rho c_p u_\tau)$ and viscous scale $y_\nu = \nu/u_\tau$. Figures 4a and 4b show how semi-local scaling allows to take into account fluid property variations in the wall-normal direction and make velocity profiles collapse to those with constant properties of Kawamura *et al.* (1999). Similar results are shown for mean and r.m.s. temperature profiles in figure 5, where $T_{rms}^{+/*} = T_{rms}/T_\tau$ and $\overline{T}^{+/*} = \left(T_w - \overline{T}\right)/T_\tau$, and the friction temperature $T_\tau = q_w/(\rho_w c_{p_w} u_\tau)$ is used for the classic wall-scaled temperatures. Fluid mean property variations seem to be the only remarkable impact of the heated wall on the flow, as suggested by Morkovin (1962) and seen in several studies concerning compressible flows (e.g. Huang & Coleman 1994; Huang *et al.* 1995; Nicoud 1999). This is supported by results shown in figure 6, where the mean wall-normal velocity, normalised with respect to the mean streamwise velocity and the friction velocity is plotted. Indeed, if the continuity equation (2.1) and the absence of streamwise gradients guarantee that the Favre-averaged normal velocity $\widetilde{v}$ is zero, mean density variations do generate ejection events in the boundary layer. Nevertheless the mean normal velocity is at most of the order of 1% and 1‰ with respect to the friction velocity and the mean streamwise velocity, respectively. Figure 7 shows the total shear stress as well as the total heat flux

$$q^{tot} = -\overline{\lambda\frac{\partial T}{\partial y}} + \overline{\rho}\widetilde{v''h''} - \int_0^y \overline{\boldsymbol{\tau} : \nabla \mathbf{v}}\ \mathrm{d}y\ .$$

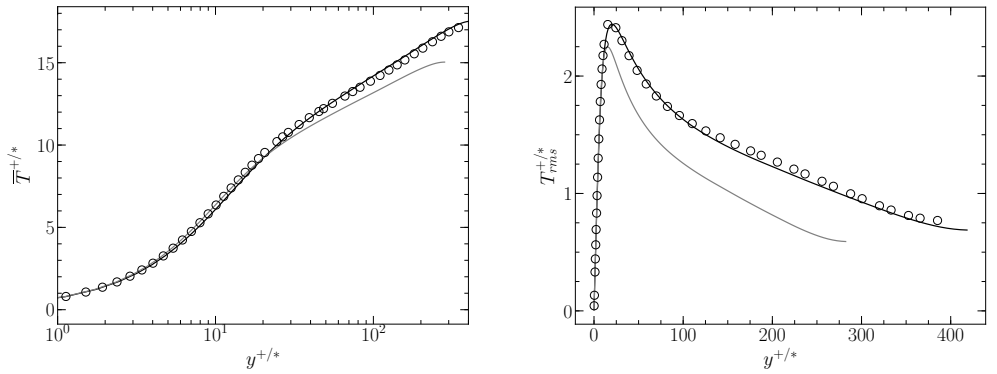

(a) (b)

Figure 5: Profiles of mean (a) and r.m.s. (b) temperature: —— present results in classic (gray) and semi-local (black) scaling; ○ results from Kawamura *et al.* (1999).

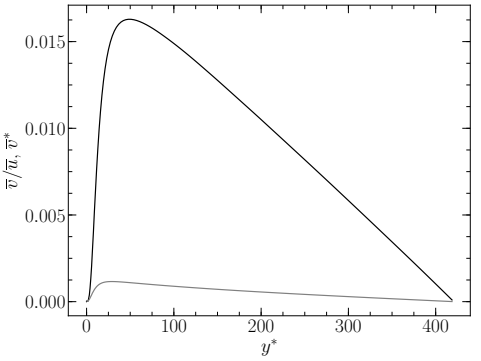

Figure 6: Wall-normal velocity normalised with respect to the friction velocity $\overline{v}^*$ (black line) and mean streamwise velocity $\overline{v}/\overline{u}$ (gray line).

Notice that the viscous heating contribution is not strictly zero even if small due to the low Mach number of the simulated flow.
Finally, figure 8 shows turbulent budgets for $\widetilde{h''^2}$ and wall-normal heat flux $-\overline{\rho}\widetilde{v''h''}$ (normalised with respect to $\overline{q_w}^2/\mu_w$ and $\overline{q_w}.\overline{\tau_w}/\mu_w$ respectively) compared to those of Kawamura *et al.* (1999). A good agreement is obtained although not as precise as in previous figures. The slight differences can be attributed to small compressibility effects in the present case and variable properties effects that the semi-local scaling most likely does not correct in these budgets. Finally, remaining numerical errors in both computations is another possible source of disagreement.

4. Results

Results for the configuration described in §2 are now presented. In the following, as in section §3, $\overline{(\cdot)}$ and $\widetilde{(\cdot)}$ denote Reynolds and Favre averages while $(\cdot)'$ and $(\cdot)''$ denote their respective fluctuating parts. Spatially, quantities are only averaged along the Z axis, which is the only homogeneous direction for this configuration.
Apex $(\cdot)^+$ denotes classic wall scaling while $(\cdot)^*$ denotes semi-local scaling. Given the streamwise evolution of the boundary layer, unless specified, scaling of quantities (dimen-

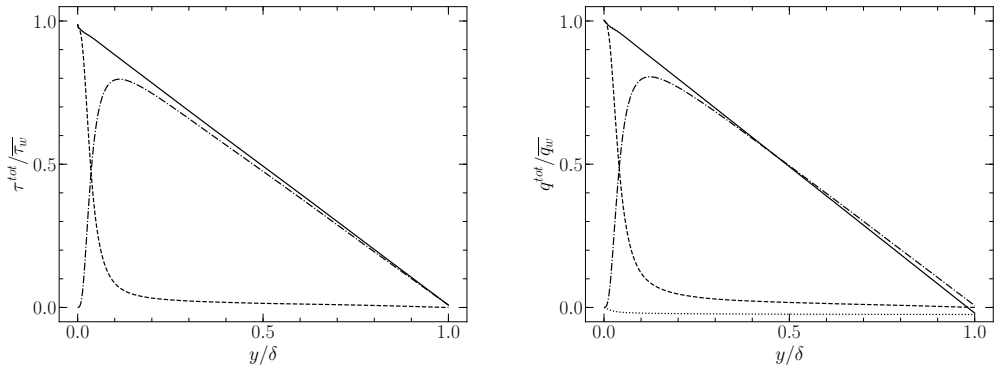

(a) (b)

Figure 7: Profiles of shear stress scaled by the wall shear stress (a): —— total shear stress τ^{tot} ; - - - - viscous term $\overline{\tau_{12}} = \overline{\mu \frac{\partial u}{\partial y}}$; – · – · – turbulent term $-\overline{\rho}\widetilde{u''v''}$.
Heat fluxes scaled by the wall heat flux (b): —— total heat flux q^{tot}; - - - - conductive term $\overline{q}_y^{cd} = -\overline{\lambda \frac{\partial T}{\partial y}}$; – · – · – turbulent term $\overline{\rho}\widetilde{v''h''}$; ····· viscous heating term $-\int_0^y \overline{\boldsymbol{\tau} : \nabla \mathbf{v}}\, \mathrm{d}y$.

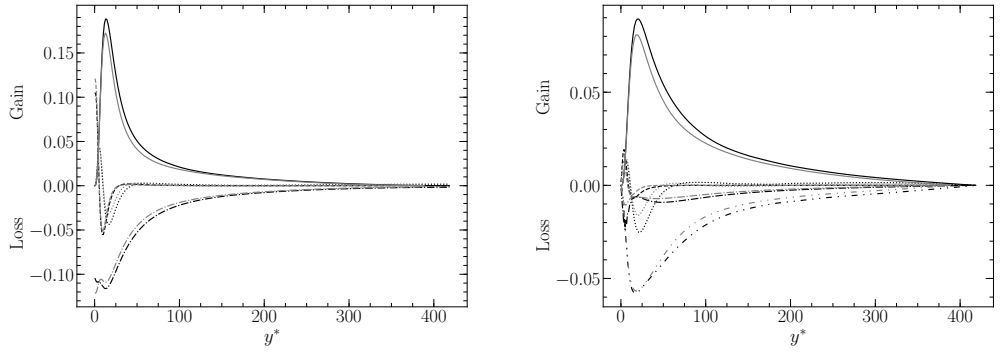

(a) (b)

Figure 8: Budgets of enthalpy variance (a) and wall-normal turbulent heat flux (b), present results (black) and Kawamura *et al.* (1999) (gray): —— production ; – · – · – molecular dissipation; - - - - molecular diffusion; ····· turbulent diffusion; – · · – enthalpy-pressure-gradient correlation.

sionless numbers included) has to be intended *locally* with respect to the X coordinate, for instance:

$$\overline{T}^{+}(y)|_{x=\xi} = \frac{T_w - \overline{T}(y)|_{x=\xi}}{T_\tau|_{x=\xi}}.$$

The origin of the axes is placed at the interface between the adiabatic and the isothermal wall so that the adimensionalised X coordinate x/δ is defined in the range $[-4\pi, 18\pi]$ between the inlet and the outlet.
The subscripts $(\cdot)_w$ and $(\cdot)_c$ indicate that the given property is evaluated at the wall and at the centre of channel, respectively, and also in this case, unless differently specified, it has to be intended locally with respect to the X coordinate.

The section is organised as follows. In section §4.1, the computation is first validated with respect to the equilibrium states described in section §3; then, in section §4.2 the

impact of the heated wall on the velocity boundary layer is analysed and the evolution of the different contributions to the momentum balance is shown; in section §4.3, the evolution of the mean temperature is shown, the averaged energy equation is introduced and the evolution of the different contributions to the total heat flux is detailed; in section §4.4, the same is done for the enthalpy variance and for the wall-normal turbulent heat flux; finally, in section §4.5 the evolution of the turbulent Prandtl number along the channel flow is investigated.

4.1. *Equilibrium states and validation*

First of all, it is necessary to verify that the configuration described in §2 allows to meet the scope of the study, that is analysing the evolution of a fully developed, adiabatic, temperature-homogeneous boundary layer at equilibrium towards a new equilibrium state characterised by a fully developed thermal boundary layer. In order to do so, two aspects have to be verified: first, that the boundary layer at $x/\delta \approx 0$ is at equilibrium and matches with results presented in §3.1; second, that the boundary layer at the outlet is again at equilibrium and matches with results shown in §3.2.

Figure 9 shows the mean streamwise velocity and the three r.m.s. velocity profiles at $x/\delta = -0.1\pi$ and $x/\delta = \frac{287}{16}\pi$, *i.e.*, slightly upstream of the interface between the adiabatic and the isothermal walls and very close to the outlet, compared to results shown in sections §3.1 and §3.2 for the two equilibrium states. At $x/\delta \approx 0$, excellent agreement on the mean streamwise velocity is obtained with respect to reference results of §3.1. Thus, the flow reaching the downstream part of the domain is a fully developed, turbulent, temperature-homogeneous boundary layer as desired. On the other hand, even though good agreement is obtained for the wall-normal and spanwise r.m.s. velocities, a disparity of around 10% is observed for the streamwise r.m.s. velocity in the log layer.
At $x/\delta \approx 18\pi$, very good agreement is obtained on both mean streamwise velocity and r.m.s. velocities with respect to results shown in §3.2 for the fully developed thermal boundary layer. The aforementioned disparity seems thus to be due to the ongoing perturbation of the recycling described in §2.2, whose effect disappears at a certain distance from it.

Figure 10 shows the mean and r.m.s. temperature profiles at $x/\delta \approx 18\pi$. Very good agreement is obtained with reference results of §3.2 on the mean temperature while a slight disparity is observed on the r.m.s profile. Thus, if on the one hand the average thermal boundary layer seems to be fully developed at the outlet, on the other hand a longer isothermal wall would have been necessary to observe the same level of convergence for temperature fluctuations.

Figure 11 shows the evolution of the Nusselt number Nu and of the heat flux parameter B_q along the channel flow compared to their respective values at equilibrium computed for the configuration described in §3.2 and summarised in table 3. As expected, Nu and B_q are both very important at the leading edge but converge towards equilibrium before the exit of the domain.

These results confirm that the given configuration and the numerical set-up allow to meet the aim of the study.

4.2. *Velocity profiles and momentum balance*

As mentioned in §2.1, temperature is not a passive scalar in (2.1), (2.2) and (2.3) and the impact of the temperature gradient on the velocity fields and momentum balance is here evaluated.
On the one hand, the heat flux parameter at equilibrium B_q^{eq} is small and so is the

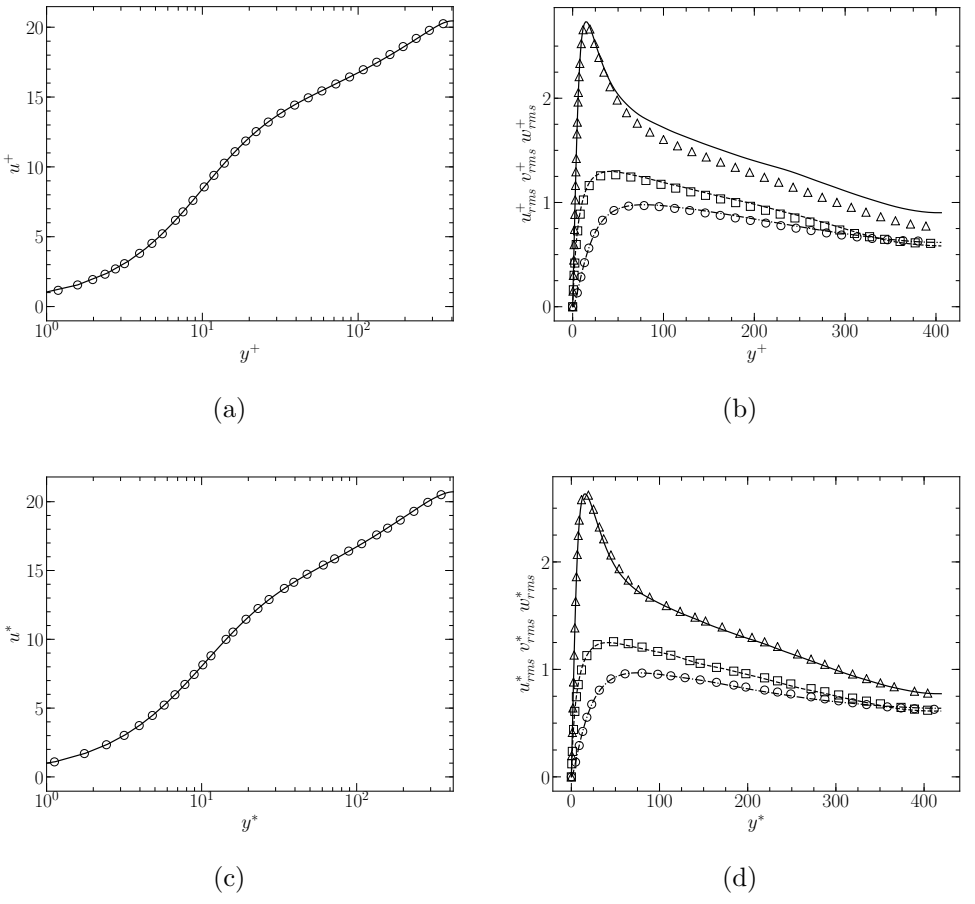

Figure 9: Mean profile of streamwise velocity (a)-(c): —— present results at $x/\delta \approx 0$ (resp. $x/\delta \approx 18\pi$); ○ reference results from §3.1 (resp. §3.2).
Profiles of r.m.s. streamwise, wall-normal and spanwise velocity respectively (b)-(d): — —, – · – · – and - - - - present results at $x/\delta \approx 0$ (resp. $x/\delta \approx 18\pi$); △, ○ and □ reference results from §3.1 (resp. §3.2).

temperature ratio between the wall and the centre of the channel. As it is showed *a priori* in §3 and *a posteriori* in §4.1, the impact is limited to a small ejection event and a variation of the mean and r.m.s. velocity profiles which collapse on the standard profiles once the semi-local scaling is used.
On the other hand, as it is shown in figure 11, there is a portion of the channel flow near the leading edge where the heat flux parameter is elevated and the impact on the boundary layer is expected to be more important. Furthermore, since the flow is subsonic, any perturbation given by the isothermal wall is also expected to slightly modify the upstream conditions.

Figure 12a shows the mean streamwise velocity for x/δ ranging between $[-0.06, 0.18]$ compared to the canonical profiles seen in section §3. Even if semi-local scaling is used, none of the profiles agrees with the equilibrium ones, showing that at these close distances from the leading edge the perturbation cannot be ascribed to the only variation of mean fluid properties. This is particularly true for the profile at $x/\delta = 0.015$, for which the velocity boundary layer seems to be at equilibrium only for $y^* \lesssim 2$, *i.e.*, in the viscous

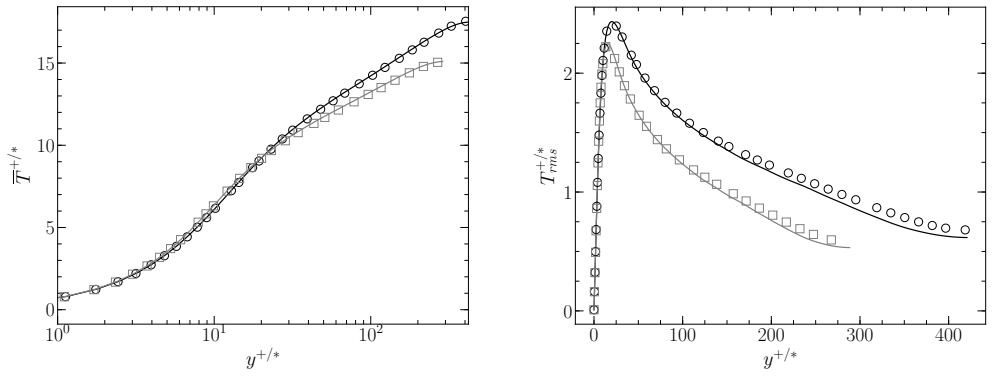

(a) (b)

Figure 10: Profiles of mean (a) and r.m.s. (b) temperature: —— present results at $x/\delta \approx 18\pi$ in classic (gray) and semi-local (black) scaling; □ (resp. ○) reference results from §3.2 in classic (resp. semi-local) scaling.

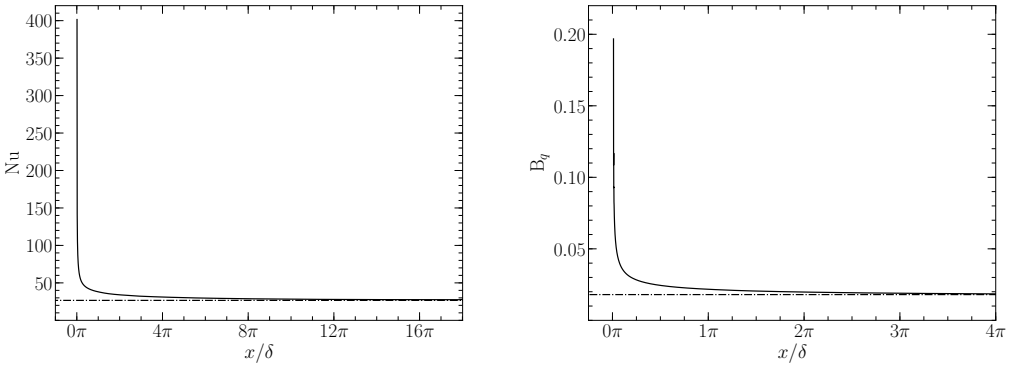

(a) (b)

Figure 11: Nusselt number Nu (a) and heat flux parameter B_q (b) as a function of x/δ: —— present results; – · – · – equilibrium values computed for the configuration of section §3.2.

sub-layer. The discrepancy of the profile at $x/\delta = -0.06$ with respect to the equilibrium profile of §3.1, instead, shows how the perturbation propagates upstream.

The same impact on the streamwise velocity was observed by Sanchez *et al.* (2014) with a lower Reynolds number and a higher temperature ratio. They showed how it is possible to make the different velocity profiles collapse once the Van Driest transformation $u^+_{VD} = \int_0^{u^+} \sqrt{\rho/\rho_w}\, \mathrm{d}u^+$ is adopted. They argued that the perturbation observed on the streamwise velocity is due to the increase of the wall-normal velocity induced by the temperature gradient and that the Van Driest transformation can take this effect into account as it is mathematically analogous, as shown by Nicoud & Bradshaw (2000), to the transformation for incompressible turbulent wall flows with uniform injection (see Simpson 1970).

If this curious mathematical analogy, as underlined by the same Nicoud & Bradshaw (2000), is unlikely to have any physical meaning, it is true that the Van Driest transformation, including the influence of the heat flux parameter (see Nicoud & Bradshaw

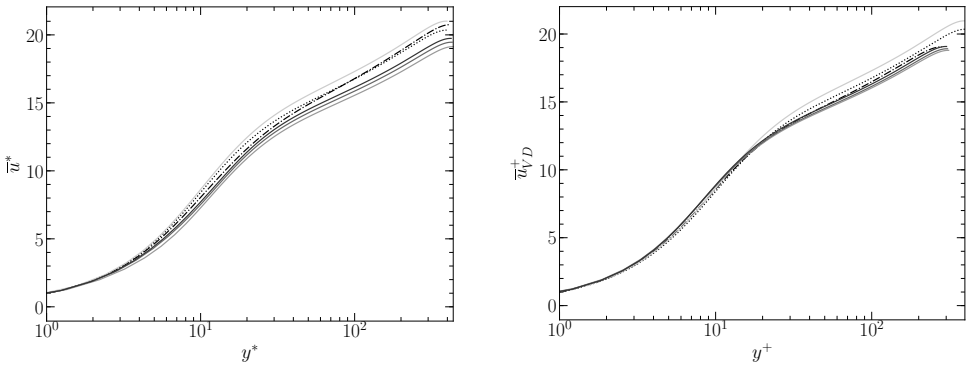

(a) (b)

Figure 12: Mean streamwise velocity profile for different x/δ in semi-local (a) and Van Driest (b) scaling: —— present results at $x/\delta = -0.06,\ 0.015,\ 0.09,\ 0.18$ (from lightest to darkest respectively); ····· equilibrium profile of section §3.1; – · – · – equilibrium profile of section §3.2.

2000), takes into account fluid property variations differently from semi-local scaling. Figure 12b shows the Van Driest-transformed streamwise velocity profiles at the same crosswise sections of figure 12a. Good agreement is obtained between the different profiles until the end of the buffer layer (*i.e.*, $y^+ \approx 20$) and the profiles downstream of the leading edge better collapse on each other as well as on the equilibrium profile of section §3.2. On the other hand, none of the profiles collapses on the equilibrium adiabatic profile of section §3.1. Furthermore, the Van Driest transformation has obviously no effect on the profile at $x/\delta = -0.06$, where the wall is adiabatic and fluid properties are thus constant along the normal direction.

At this stage, we cannot exclude that the wall-normal velocity is responsible for the perturbation of the mean streamwise velocity. It is certainly true that the wall-normal velocity considerably increases near the leading edge, as it can be seen in figures 13a and 13b. The peak of Y velocity can attain 10% of the local friction velocity and 1% of the local mean streamwise velocity. Yet, one can also observe that the wall-normal velocity is relatively important at $x/\delta = -0.06$ and, above all, always greater than zero. If the wall-normal velocity were the only responsible for the deviation of the streamwise velocity profile, the impact would be expected to be similar to the one observed downstream of the leading edge, where the normal velocity is also always positive and of the same order of magnitude. Instead, as it can be seen in figure 12a, it is not the case, since the streamwise velocity at $x/\delta = -0.06$ and, for example, $x/\delta = 0.18$ are respectively above and below the canonical log law.

Hence, we propose a different interpretation, *i.e.*, that the destabilisation of the boundary layer is due to to the abrupt variation of the wall shear stress. Figure 14a shows the evolution of the skin friction coefficient $C_f = \overline{\tau_w} / \left(\frac{1}{2}\rho_b u_b^2\right)$ where ρ_b and u_b are respectively the bulk density and the bulk velocity.

At $x/\delta = 0^+$ the skin friction coefficient is at its maximum, which can be explained by the abrupt increase of the fluid dynamic viscosity at the leading edge of the isothermal wall. Then, the following relaxation and adaptation of the velocity gradient at the wall to the increased viscosity leads to a quickly decreasing C_f until it attains a plateau.

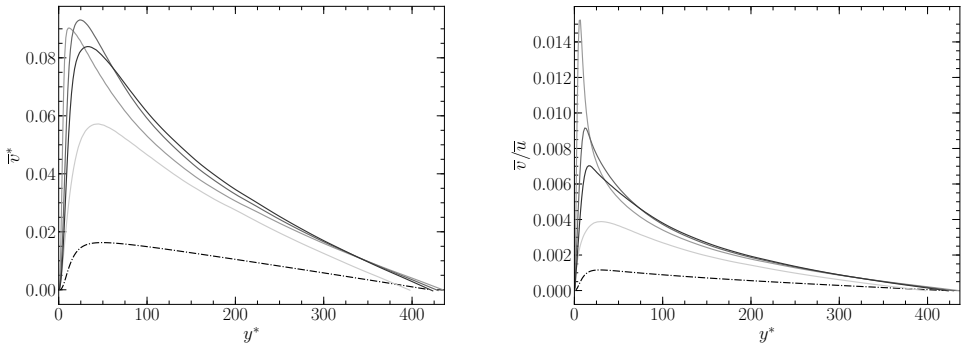

(a) (b)

Figure 13: Wall-normal velocity profile for different x/δ in semi-local scaling (a) and non-dimensionalised with respect to the mean streamwise velocity(b): —— present results at $x/\delta = 0.015 - 0.18 - 0.73$ (from lightest to darkest respectively); – · – · – equilibrium profile of section §3.2.

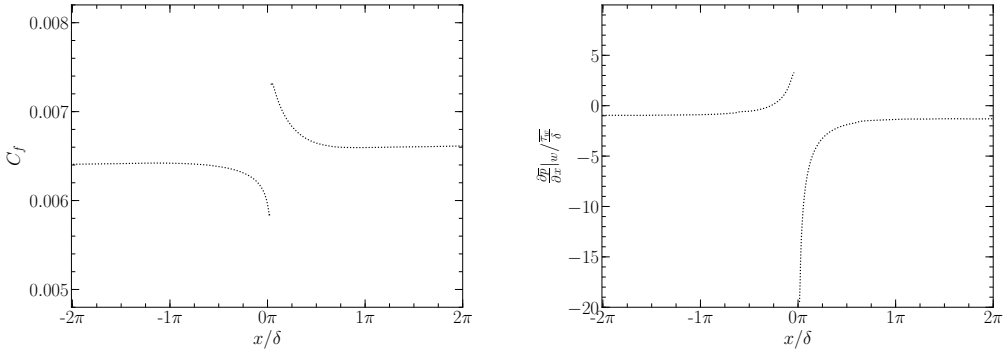

(a) (b)

Figure 14: Skin friction coefficient C_f (a) and non-dimensionalised wall pressure gradient (b) along the channel flow.

At $x/\delta = 0^-$, instead, the skin friction coefficient is at its minimum. This effect is due to the fact that the flow, being subsonic, perceives the upcoming isothermal wall and adapts by decreasing the gradient of the streamwise velocity at the wall while the dynamic viscosity is constant since the wall is adiabatic.
This perturbation, limited to a very small portion of the channel flow between $x/\delta \in [-\frac{1}{2}\pi, \frac{1}{2}\pi]$, results in a local perturbation of the wall streamwise pressure gradient, as it can be seen in figure 14b non-dimensionalised with respect to the ratio $\overline{\tau_w}/\delta$. While $\frac{\partial \overline{p}}{\partial x}|_w / \frac{\overline{\tau_w}}{\delta} \approx -1$ far from the leading edge, a positive (and thus adverse) and strongly negative (and thus favourable) pressure gradient is observed at $x/\delta = 0^-$ and $x/\delta = 0^+$, respectively.
In order to take the effect of the streamwise pressure gradient into account, we introduce, following Simpson (1983), the velocity scale u_p defined as:

$$u_p = \left| \frac{\mu}{\rho^2} \frac{\partial p}{\partial x}\Big|_w \right|^{\frac{1}{3}} \tag{4.1}$$

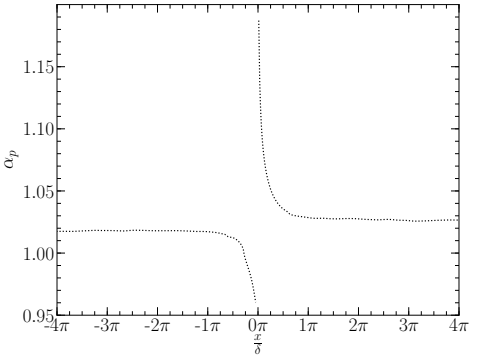

Figure 15: Ratio of scale velocities $\alpha_p = u_\tau^2/u_{\tau p}^2$.

which, combined with the classic friction velocity $u_\tau = |\tau_w/\rho|^{\frac{1}{2}}$, gives as proposed by Manhart *et al.* (2008):

$$u_{\tau p} = \sqrt{u_\tau^2 + u_p^2} \ . \tag{4.2}$$

We propose here a slight modification of this definition, which allows do distinguish between positive and negative pressure gradients:

$$u_{\tau p} = \sqrt{u_\tau^2 + \text{sign}\left(\frac{\partial p}{\partial x}\Big|_w\right) u_p^2} \ . \tag{4.3}$$

In this manner, the decrease of u_τ in case of adverse pressure gradient and its increase in case of favourable pressure gradient are compensated by u_p, correcting the upward and downward deviation of the streamwise velocity profile respectively upstream and downstream of the leading edge observed in figure 12a. Figure 15 shows the evolution of the scale velocity ratio $\alpha_p = u_\tau^2/u_{\tau p}^2$, as defined by Manhart *et al.* (2008), in proximity of the leading edge. It can be seen that α_p varies between approximately 0.95 and 1.2, values close to unity which nevertheless indicate that the pressure gradient is not negligible.

We can thus introduce the following wall scaling:

$$\begin{aligned} y_{\tau p}^* &= \tfrac{y u_{\tau p}}{\nu} \\ u_{\tau p}^* &= \frac{u}{u_{\tau p}} \ , \end{aligned} \tag{4.4}$$

where, analogously to semi-local scaling, fluid properties depend on the wall-normal direction in order to take the effect of the temperature gradient into account.

Figure 16a shows the same velocity profiles of figures 12a and 12b in the newly introduced wall scaling while figure 16b shows the r.m.s. velocity profiles. Very good agreement is obtained between the different profiles in every zone of the boundary layer, with the only exception of the r.m.s. streamwise velocity, for which the deviation in the log layer from the equilibrium profile of section §3.2 has to be ascribed in any case to what is explained in section §4.1 and shown in figure 9.

In order to well understand the impact of the isothermal wall on the velocity fields near the leading edge, the evolution of the different terms of the momentum balance has to be analysed. For every crosswise section, integrating along the wall-normal direction

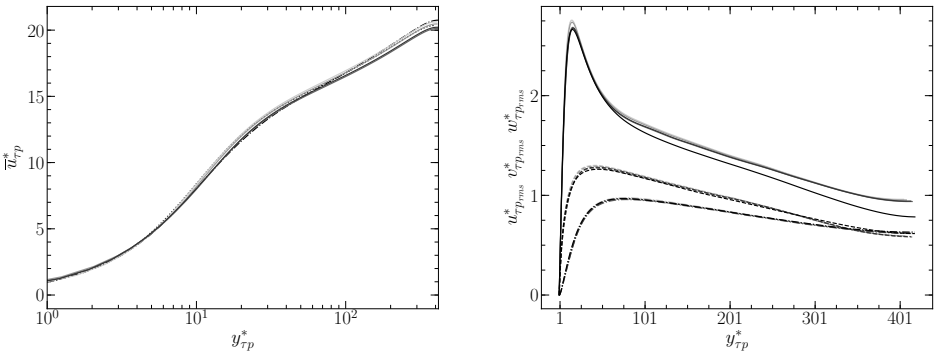

(a) (b)

Figure 16: Mean streamwise velocity profile for different x/δ in the newly introduced wall scaling (see (4.4)) (a): —— present results at $x/\delta = -0.06,\ 0.015,\ 0.09,\ 0.18$ (from lightest to darkest respectively); ····· equilibrium profile of section §3.1; – · – · – equilibrium profile of section §3.2.
Profiles of r.m.s. streamwise, wall-normal and spanwise velocity respectively for different x/δ in the newly introduced wall scaling (see (4.4)) (b): ——, – · – · – and - - - - present results at (from light gray to black) $x/\delta = -0.06,\ 0.015,\ 0.09,\ 0.18$ and equilibrium (see §3.2).

the local momentum balance gives:

$$\begin{aligned}\overline{\tau}_w(x) = &-\underbrace{\int_0^y \left(\overline{\rho}\widetilde{u}\frac{\partial \widetilde{u}}{\partial x}\right)\mathrm{d}y}_{I_x} - \underbrace{\int_0^y \left(\overline{\rho}\widetilde{v}\frac{\partial \widetilde{u}}{\partial y}\right)\mathrm{d}y}_{I_y} - \underbrace{\int_0^y \left(\frac{\partial \overline{p}}{\partial x}\right)\mathrm{d}y}_{II} + \\ &+\underbrace{\int_0^y \left(\frac{\partial \overline{\boldsymbol{\tau}_{xx}}}{\partial x}\right)\mathrm{d}y}_{III_x} + \underbrace{\overline{\boldsymbol{\tau}_{xy}}(y)}_{III_y} + \\ &-\underbrace{\int_0^y \left(\frac{\partial}{\partial x}\left(\overline{\rho}\widetilde{u''u''}\right)\right)\mathrm{d}y}_{IV_x} - \underbrace{\overline{\rho}\widetilde{u''v''}(y)}_{IV_y},\end{aligned} \tag{4.5}$$

where on the right-hand side of the equation there are two mean convective terms (I_x and I_y), the pressure gradient (II), two viscous terms (III_x and III_y) and two terms associated with turbulent transport (IV_x and IV_y). The fully developed regime yields the familiar flux balance:

$$\overline{\tau}_w + y\frac{\mathrm{d}p}{\mathrm{d}x} = \overline{\boldsymbol{\tau}_{xy}}(y) - \overline{\rho}\widetilde{u''v''}(y) \quad \text{or} \quad \overline{\tau}_w\left(1-\frac{y}{\delta}\right) = \overline{\boldsymbol{\tau}_{xy}}(y) - \overline{\rho}\widetilde{u''v''}(y). \tag{4.6}$$

Figure 17 shows the different terms non-dimensionalised with respect to the average local wall shear stress $\overline{\tau_w}$ as a function of y/δ for different values of x/δ.
Figure 17a is relative to $x/\delta = -0.06$. At this close distance from the leading edge, the terms of (4.5) are strongly perturbed. The pressure gradient flux does not follow a straight line, showing that $\partial\overline{p}/\partial x$ is not uniform along the wall-normal direction and that the pressure field is bidimensional; it is also evident how the streamwise pressure gradient is positive (and thus adverse) but only in a very limited portion of the boundary layer, until $y/\delta \approx 0.05$. Both mean convective terms are important; the positive slope of the

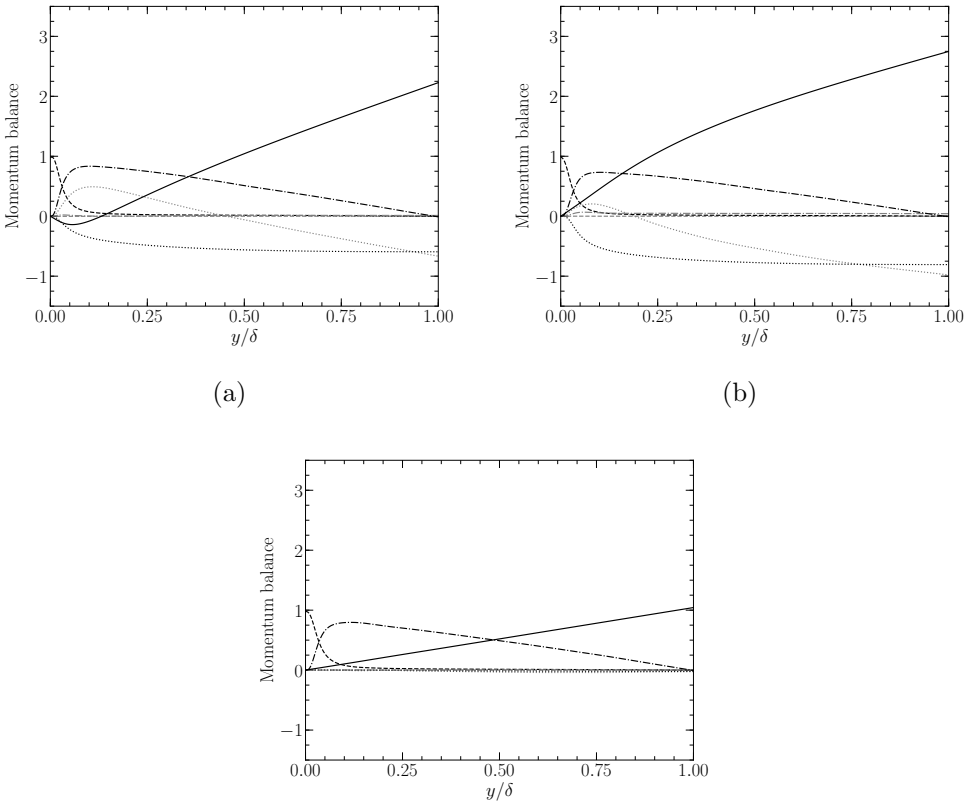

Figure 17: Momentum flux balance at $x/\delta = -0.06$ (a), 0.18 (b), and 5π (c): —— pressure gradient; - - - - streamwise (gray) and wall-normal (black) viscous terms; ····· streamwise (gray) and wall-normal (black) mean convective terms; – · – · – streamwise (gray) and wall-normal (black) turbulent terms.

streamwise convective term near the wall indicates that $\partial\widetilde{u}/\partial x$ is negative, resulting in the aforementioned decrease of the wall shear stress; the negative slope of the wall-normal convective term shows how $\widetilde{v}$ is everywhere greater than or equal to zero. The remaining terms, like the wall-normal viscous term and the wall-normal turbulent flux, seem not to be significantly modified, indicating that the perturbation of the pressure gradient is fully compensated by the two convective terms. This seems to confirm the hypothesis that the non-equilibrium contributions to the momentum balance tend to self-compensate (see Larsson *et al.* 2016); yet, as the pressure gradient needs to be nevertheless taken into account for correcting the velocity profiles, it is evident how these non-equilibrium terms can affect independently the flow's mean quantities, and, therefore, need to be considered regardless of whether they balance each other or not.

Figure 17b is relative to $x/\delta = 0.18$. The pressure gradient flux still does not follow a straight line and the pressure field is thus bidimensional; the positive slope of the pressure gradient term indicates that $\partial\overline{p}/\partial x$ is now negative for every y/δ. Both mean convective terms are still important; near the wall, like at $x/\delta = -0.06$, $\partial\widetilde{u}/\partial x < 0$, indicating that the wall shear stress is decreasing.

Figure 17c, finally, is relative to $x/\delta = 5\pi$, *i.e.*, relatively far from the leading edge,

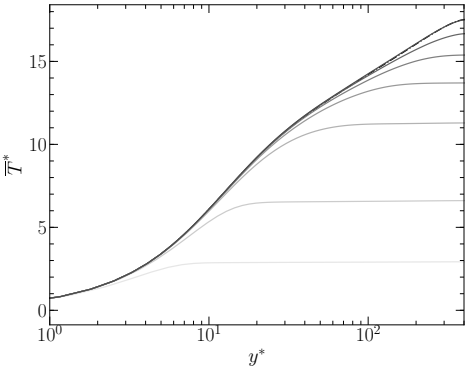

Figure 18: Profiles of mean temperature in semi-local scaling for different x/δ: —— present results at $x/\delta = 0.015$ - 0.21 - $\frac{1}{2}\pi$ - $\frac{3}{2}\pi$ - 3.6π - 7.75π - 17.9π (from lighter to darker); – · – · – equilibrium profile of section §3.2.

where the skin friction coefficient, the wall streamwise pressure gradient and the heat flux parameter have all stabilised. As can be seen, the canonical momentum fluxes are retrieved, with, in particular, a linear pressure term evolving from zero to unity, which is associated with the homogeneous pressure gradient.

In conclusion, the impact of the sudden isothermal wall condition on the velocity field can be summarised as follows. The abrupt variation (and, in this case, increase) of wall temperature at the leading edge leads to a variation of the dynamic viscosity and of the mass density. As a consequence, the wall shear stress is perturbed (see Fig. 14a) and so is the velocity field: near the wall $\partial\overline{u}/\partial y$ decreases to adapt to the new dynamic viscosity and the wall-normal velocity increases by mass conservation; the same impact is slightly propagated upstream, since the flow is subsonic. As a result, the pressure field is perturbed in the very proximity of the wall, with an adverse streamwise pressure gradient developing upstream of the leading edge (see Fig. 14b).

In order to correct the effect of the pressure gradient, the scaling velocity and viscous length are modified as shown in Eq. (4.4), which allows to make the mean streamwise and r.m.s. streamwise, wall-normal and spanwise velocity profiles to collapse on the classic equilibrium ones.

Further away from the leading edge, where the skin friction coefficient, the wall streamwise pressure gradient and the heat flux parameter have all stabilised, the classic momentum fluxes are retrieved, $u_{\tau p} \approx u_\tau$ and the only effect on the velocity boundary layer induced by the temperature gradient is given by the variation of mean fluid properties which can be taken into account through semi-local scaling.

4.3. *Mean temperature profiles and energy balance*

Since the temperature profile of the flow making contact with the isothermal wall is uniform, it is undoubtedly on the temperature that the impact of the heated wall is more important. The goal of this section is to describe the development of the thermal boundary layer from the leading edge to the outlet and to identify, thanks to the evolution of the terms composing the energy balance, the different non-equilibrium regions of the flow.

The progressive development of the thermal boundary layer along the channel flow in the present case is shown in figure 18, where several mean temperature profiles are plotted at different x/δ and compared to the equilibrium profile of section §3.2.

For every x/δ, three distinct parts of the developing thermal boundary layer can be identified. The first is the near wall region where, for $y^* \in [0, h^*_{eq}]$ where h^*_{eq} depends on and increases with x/δ, the thermal boundary layer is fully developed and the mean temperature profile agrees with the one at equilibrium; the second, for $y^* \in [h^*_{n-eq}, \delta^*]$ where h^*_{n-eq} also depends and increases with x/δ, is a region that is still not affected by the isothermal wall and the temperature profile is flat; the third, for $y^* \in [h^*_{eq}, h^*_{n-eq}]$, is instead the actual non equilibrium developing portion of the thermal boundary layer, where the mean temperature profile is neither flat nor agreeing with the equilibrium one. As x/δ increases, both h^*_{eq} and h^*_{n-eq} tend towards the mid-height of the channel δ^* and the non equilibrium region disappears.

The existence of an equilibrium layer in the development of the thermal boundary layer has been shown experimentally, for example by Blom (1970) (who called this zone *adapted region*) or Teitel & Antonia (1993) for a step change in temperature and wall heat flux, respectively. The objective is to analyse the evolution of the equilibrium layer (delimited by h^*_{eq}) and of the non-equilibrium region (delimited by h^*_{n-eq}) yet, to do so, it is necessary to quantitatively define the notions of *equilibrium* and *non-equilibrium*. We propose to do so through the analysis of the different terms of the energy balance. The integration along the wall-normal direction of the local averaged energy equation gives a local heat budget for every crosswise section:

$$\begin{aligned}\overline{q}_w(x) = &\underbrace{\int_0^y \left(\overline{\rho}\widetilde{u}\frac{\partial \widetilde{h}}{\partial x}\right)\mathrm{d}y}_{I_x} + \underbrace{\int_0^y \left(\overline{\rho}\widetilde{v}\frac{\partial \widetilde{h}}{\partial y}\right)\mathrm{d}y}_{I_y} + \underbrace{\int_0^y \left(\frac{\partial \overline{q_x^{cd}}}{\partial x}\right)\mathrm{d}y}_{II_x} + \underbrace{q_y^{cd}}_{II_y} + \\ &+ \underbrace{\int_0^y \left(\frac{\partial}{\partial x}\left(\overline{\rho}\widetilde{u''h''}\right)\right)\mathrm{d}y}_{III_x} + \underbrace{\overline{\rho}\widetilde{v''h''}}_{III_y} - \underbrace{\int_0^y \left(\frac{\mathrm{D}\overline{p}}{\mathrm{D}t} + \overline{\boldsymbol{\tau} : \nabla \mathbf{v}}\right)\mathrm{d}y}_{IV} - \underbrace{yS_{ener}}_{V}, \quad (4.7)\end{aligned}$$

where on the right-hand side of the equation there are two mean convective terms (I_x and I_y), two mean conductive terms (II_x and II_y), two terms associated with turbulent heat transport (III_x and III_y), one flux combining compressibility effects, *i.e.*, the pressure material derivative and the viscous dissipation (IV) and the source term contribution (V). The fully developed regime for low Mach-number flows yields the familiar heat flux balance:

$$\overline{q}_w + yS_{ener} = q_y^{cd} + \overline{\rho}\widetilde{v''h''} \quad \text{or} \quad \overline{q}_w\left(1 - \frac{y}{\delta}\right) = q_y^{cd} + \overline{\rho}\widetilde{v''h''}. \quad (4.8)$$

Figure 19 shows the evolution of the different fluxes, non-dimensionalised with respect to the average wall heat flux $\overline{q}_w(x)$, as a function of y/δ for different crosswise sections. The first remark which can be made is that certain contributions, such as the streamwise conductive flux and the compressibility effects, are negligible for every x/δ. Consequently, they will not be discussed here.

Figure 19a is relative to $x/\delta = 0.73$. At this short distance from the leading edge, many contributions, which do not appear in bi-periodical channel flows at equilibrium, are important. It is the case, for example, of the wall-normal convective flux since at this crosswise section, as it is shown in figure 13, the peak of the mean wall-normal velocity is considerably higher compared to equilibrium. It is also the case of the streamwise turbulent flux, indicating that the correlation $\widetilde{u''h''}$ is evolving and increasing (in module) close to the leading edge. Yet, the preponderant contribution is that of the streamwise convective flux. Close to the wall its slope is positive, indicating that the streamwise enthalpy gradient is positive; thus, the thermal boundary layer is developing and, as it

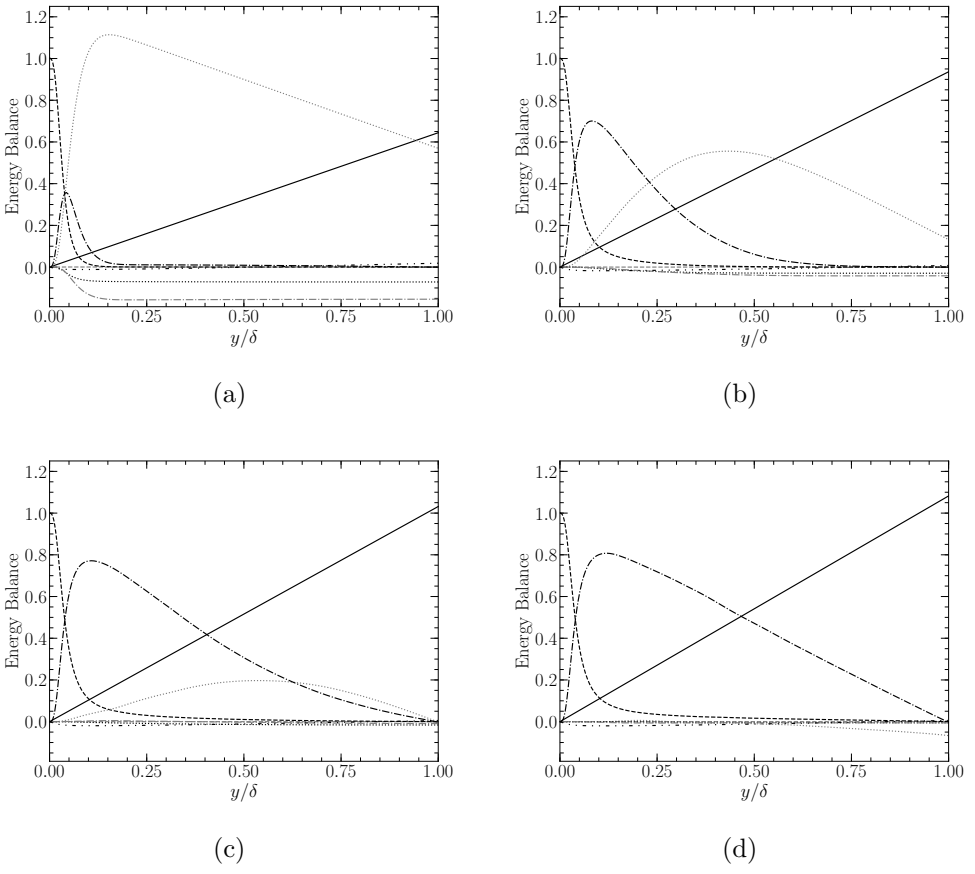

Figure 19: Energy flux balance at $x/\delta = 0.73$ (a), 2π (b), 5.7π (c) and 16.5π (d): —— source term; - - - - streamwise (gray) and wall-normal (black) conductive fluxes; ····· streamwise (gray) and wall-normal (black) convective fluxes; – · – · – streamwise (gray) and wall-normal (black) turbulent fluxes; – · · – compressibility effects.

can be seen in figure 19a, the wall-normal conductive and turbulent fluxes are active. Farther away from the wall, the slope of the streamwise convective flux is negative and linear, showing that here $\partial\widetilde{h}/\partial x$ is negative; since all the other contributions are constant, it is evident that the only active phenomenon taking place is the uniform cooling caused by the source term. It is thus a portion of the boundary layer which still has not perceived the presence of the heated wall.

Figure 19b is relative to $x/\delta = 2\pi$, where many of the observations made for $x/\delta = 0.73$ remain valid. The streamwise turbulent flux and the wall-normal convective flux are still not negligible even if substantially less important. The preponderant contribution is again that of the streamwise convective flux: as long as its slope is positive, the wall-normal conductive and turbulent fluxes are active whereas farther from the wall it is the source term imposing its negative and constant slope.

At $x/\delta = 5.7\pi$, shown in figure 19c, the streamwise turbulent flux and the wall-normal convective flux are by now negligible. The streamwise convective term, despite being still relatively important, is no more the preponderant contribution with respect to the wall-normal turbulent heat flux which has considerably grown (compare figures 19b and 19c). The fact that the wall-normal turbulent flux is different from zero everywhere but

at $y/\delta = 1$ suggests that at this crosswise section the impact of the heated wall has by now reached the centre of the channel.
At $x/\delta = 16.5\pi$ (see Fig. 19d), the classic equilibrium fluxes are retrieved. Despite this, it can be seen that near the centre of the channel the streamwise convective flux is negative and decreasing: this indicates that the temperature at $y/\delta = 1$ is still decreasing under the action of the source term and shows how even at the exit of the channel flow the thermal boundary layer is not perfectly developed given the limited extent of the simulated channel flow.

The evolution of the different contributions to the energy balance shows that the fluxes can be divided into two categories. The former is that of the *equilibrium* terms, which tend to become more and more important with x/δ until stabilisation. The contributions that belong to this category and which are encountered in bi-periodical channel flows are the wall-normal conductive flux and the wall-normal turbulent flux. The latter is that of the *non-equilibrium* terms which, even if potentially preponderant near the leading edge, tend to become negligible and disappear with x/δ. The contributions belonging to this category are the streamwise and wall-normal convective terms as well as the streamwise turbulent flux.
Now, neglecting the streamwise conductive flux as well as the compressibility effects and defining the average total heat flux q^{tot} as:

$$q^{tot} = \overline{q_w}(x) + yS_{ener} \ , \tag{4.9}$$

the sum of the equilibrium terms q^{eq} as:

$$q^{eq} = q_y^{cd} + \overline{\rho}\widetilde{v''h''} \ , \tag{4.10}$$

and the sum of the non-equilibrium terms q^{n-eq} as:

$$q^{n-eq} = \int_0^y \left(\overline{\rho}\widetilde{u}\frac{\partial \widetilde{h}}{\partial x}\right) \mathrm{d}y + \int_0^y \left(\overline{\rho}\widetilde{v}\frac{\partial \widetilde{h}}{\partial y}\right) \mathrm{d}y + \int_0^y \left(\frac{\partial}{\partial x}\left(\widetilde{\overline{\rho}u''h''}\right)\right) \mathrm{d}y \ , \tag{4.11}$$

Equation (4.7) can be rearranged in the following form:

$$q^{tot} = q^{eq} + q^{n-eq} \ . \tag{4.12}$$

For every x/δ and y/δ, it is thus possible to define the ratio:

$$R_{tot}^{n-eq} = \frac{|q^{n-eq}|}{|q^{eq}| + |q^{n-eq}|} \ , \tag{4.13}$$

quantifying the importance of the non-equilibrium terms in the energy balance.

Figure 20 shows the evolution of R_{tot}^{n-eq} along the wall-normal direction for different x/δ. The ratio R_{tot}^{n-eq} allows to define a quantitative criterion for distinguishing the three aforementioned regions of the developing thermal boundary layer. Indeed, as it can be seen in figure 20, for every x/δ there is a near-wall portion of the boundary layer where the equilibrium fluxes are predominant with respect to the non-equilibrium ones; consequently $R_{tot}^{n-eq} \approx 0$ and the energy equation can be simply approximated as

$$\overline{q_w} + yS_{ener} \approx q_y^{cd} + \widetilde{\overline{\rho}v''h''} \ .$$

The equilibrium region of the boundary layer, delimited by $h_{eq}^*(x)$, can thus be defined as the region laying beneath an isoline of R_{tot}^{n-eq} in the $x-y$ plane, for example $R_{tot}^{n-eq} = 0.1$. For every x/δ there is also a portion of the boundary layer adjacent to the centre of the channel where the non-equilibrium terms are predominant; consequently $R_{tot}^{n-eq} \approx 1$, the

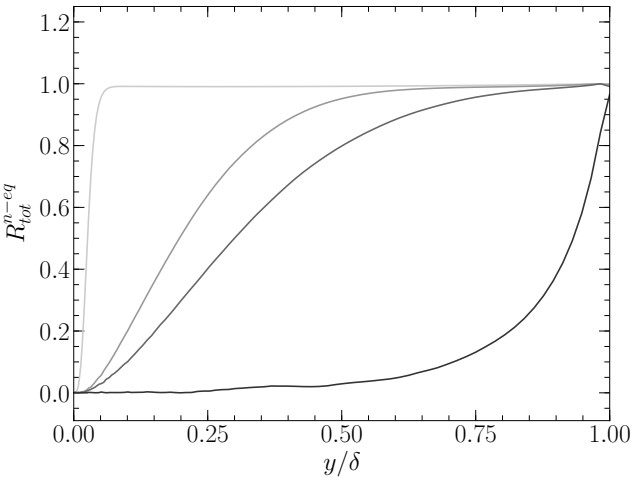

Figure 20: Evolution of R_{tot}^{n-eq} with respect to y/δ for $x/\delta = 0.18$, 1.5π, 2.5π and 16.5π (from light gray to black).

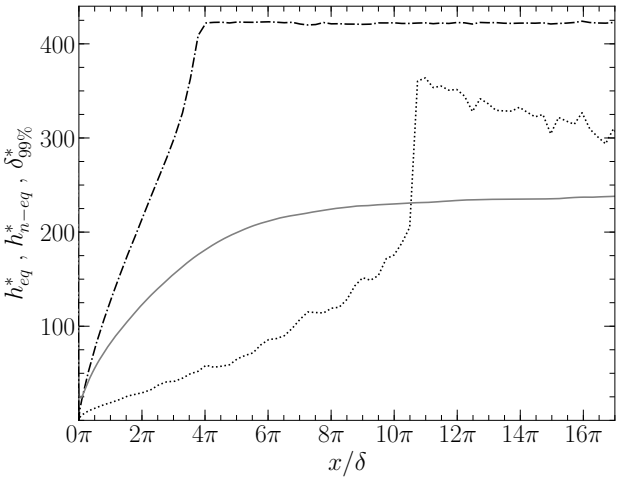

Figure 21: Evolution of h_{eq}^*, h_{n-eq}^* and $\delta_{99\%}^*$ along the channel flow: $\cdots\cdots$ h_{eq}^*; $-\cdot-\cdot-$ h_{n-eq}^*; —— $\delta_{99\%}^*$.

only active physical phenomenon is the cooling caused by the source term and the mean temperature profile is flat along the wall-normal direction. This region of the boundary layer, delimited by $h_{n-eq}^*(x)$, can thus be defined as the region laying above an isoline of R_{tot}^{n-eq}, for example $R_{tot}^{n-eq} = 0.9$.
Finally, for every x/δ and for $y^* \in [h_{eq}^*, h_{n-eq}^*]$, the equilibrium and non-equilibrium fluxes are of the same order of magnitude and the thermal boundary layer is in development.

Figure 21 shows the evolution of h_{eq}^* (defined as the isoline $R_{eq}^{n-eq} = 0.1$) and h_{n-eq}^* (defined as the isoline $R_{eq}^{n-eq} = 0.9$) compared to the wall-scaled thermal boundary layer thickness $\delta_{99\%}^* := h^* \ : \ \left|T_w - \overline{T}(h^*)\right| / \left|T_w - \overline{T}_c(x)\right| = 0.99$.
The region of the thermal boundary layer laying above h_{n-eq}^* tends to quickly disappear as h_{n-eq}^* approaches $\delta^* = \mathrm{Re}_{\tau^*} \sim 400$ before $x/\delta = 4\pi$. Downstream of this crosswise

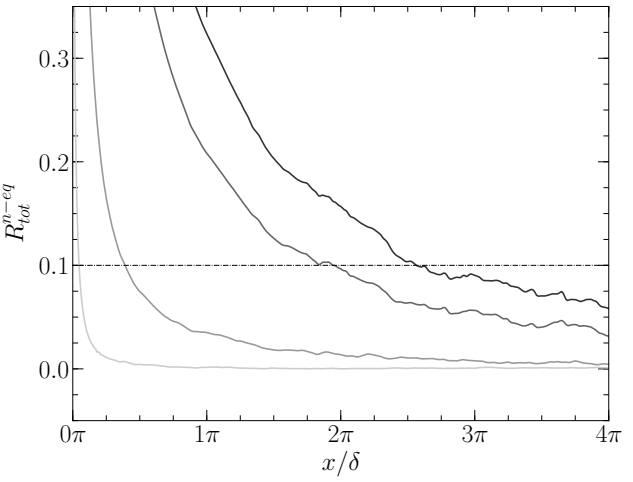

Figure 22: Evolution of R_{tot}^{n-eq} as a function of x/δ for several wall distances: —— R_{tot}^{n-eq} for $y^* = 5$, 12.5, 30 and 40 (from light gray to black respectively); – · – · – isoline $R_{tot}^{n-eq} = 0.1$.

section, the effect of the heated wall has reached the centre of the channel and, as shown in figure 18, the mean temperature profile is nowhere flat any more. As one could expect, $h_{n-eq}^* > \delta_{99\%}^*$ everywhere. The fast decay of the region beyond h_{n-eq}^* indicates a rapid wall-normal expansion of the equilibrium terms and might be due to the fact that since the velocity boundary layer is fully developed, the transport of the heated pockets of the flow towards the centre of the channel can efficiently be carried out by turbulence.
On the other hand, the increase rate of h_{eq}^* as a function of x/δ is slower. Curiously, an abrupt change in h_{eq}^* takes place at $x/\delta \approx 10\pi$ where the profile intercepts the boundary layer thickness $\delta_{99\%}^*$. Beyond, h_{eq}^* attains a peak at $y^* \approx 350$ before slowly decreasing, instead of reaching the centre of the channel. This is a portion of the boundary layer where the temperature is essentially homogeneous in the wall-normal direction, and still ruled by the cooling effect of the source term inducing a negative streamwise convective flux, which is not yet counterbalanced by the heating effect of the isothermal wall (see Fig. 19d). Hence, figure 21 shows that the structure of the thermal boundary layer is fully equilibrated for $x/\delta \gtrapprox 10\pi$, while the core flow in the channel is still subdued to some variation.

Finally, figure 22 shows the evolution of R_{tot}^{n-eq} as a function of x/δ for several wall distances. The intersection of every iso-y^* with the isoline $R_{tot}^{n-eq} = 0.1$ can be seen as the non-equilibrium distance associated to that wall distance, *i.e.*, the distance from the leading edge which is necessary for the thermal boundary layer to be at equilibrium between the wall and the specified y^*.

4.4. *Root-mean-square temperature and wall-normal turbulent heat flux: profiles and respective budgets*

Figure 23 shows the evolution of the temperature fluctuations (in semi-local scaling) and of the wall-normal turbulent heat flux (scaled with respect to the local wall heat flux) for different crosswise sections compared to the equilibrium profiles of section §3.2.

The evolution of the wall-normal turbulent heat flux in Fig. 23b is somewhat similar to

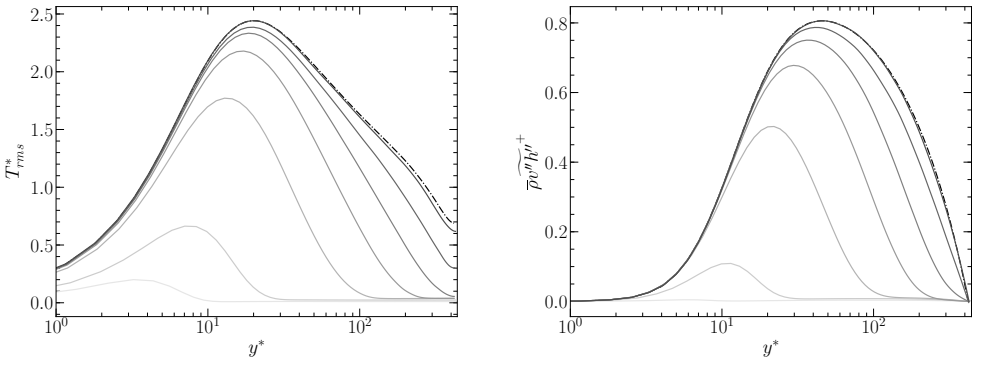

(a) (b)

Figure 23: Profiles of r.m.s temperature (a) and wall-normal turbulent heat flux (b) for different x/δ: —— present results at $x/\delta = 0.015$ - 0.21 - $\frac{1}{2}\pi$ - $\frac{3}{2}\pi$ - 3.6π - 7.75π - 17.9π (from lighter to darker); – · – · – equilibrium profiles of section §3.2.

that of the mean temperature. Indeed, for every x/δ, one can identify a near-wall region where the profile agrees with the one at equilibrium, a region which is still not affected by the isothermal wall and the profile is flat, and a region in between where the turbulent heat flux is developing.

Interestingly, the same cannot be said about the fluctuating temperature profiles in Fig. 23a. If one can identify, for every x/δ, a portion of the boundary layer where the level of the r.m.s. temperature is zero, it is only at a certain distance from the leading edge that the level of fluctuations starts agreeing with the equilibrium one. This shows how the turbulent fluctuations have a stronger inertia and need a larger distance to settle, an aspect which has also been observed experimentally (see Teitel & Antonia 1993).

Figure 23b also outlines the fast wall-normal expansion of the turbulent heat flux during the early boundary layer development mentioned previously in §4.3. This explains the fast decay of the region $y^* > h^*_{n-eq}$ seen in Fig. 21.

On the other hand, in both cases the peak shifts with x/δ towards the higher y^* until it stabilises at $y^* \approx 20$ for the r.m.s temperature and $y^* \approx 45$ for the turbulent heat flux.

The time-averaged transport equation for the enthalpy variance reads (see appendix A.1 for the detailed derivaton):

$$
\begin{aligned}
0 = &\underbrace{-\frac{\partial}{\partial x}\left(\overline{\rho}\widetilde{u}\frac{\widetilde{h''^2}}{2}\right)}_{I_x}\underbrace{-\frac{\partial}{\partial y}\left(\overline{\rho}\widetilde{v}\frac{\widetilde{h''^2}}{2}\right)}_{I_y}\underbrace{-\frac{\partial}{\partial x}\left(\overline{q_x^{cd'}h'}\right)}_{II_x}\underbrace{-\frac{\partial}{\partial y}\left(\overline{q_y^{cd'}h'}\right)}_{II_y}+\\
&+\underbrace{\overline{q_x^{cd'}\frac{\partial h'}{\partial x}}+\overline{q_y^{cd'}\frac{\partial h'}{\partial y}}+\overline{q_z^{cd'}\frac{\partial h'}{\partial z}}}_{III}+\underbrace{\overline{h'N'}}_{IV}\underbrace{-\overline{\rho}\widetilde{u''h''}\frac{\partial\widetilde{h}}{\partial x}}_{V_x}\underbrace{-\overline{\rho}\widetilde{v''h''}\frac{\partial\widetilde{h}}{\partial y}}_{V_y}+\\
&\underbrace{-\frac{1}{2}\frac{\partial}{\partial x}\left(\overline{\rho}\widetilde{u''h''h''}\right)}_{VI_x}\underbrace{-\frac{1}{2}\frac{\partial}{\partial y}\left(\overline{\rho}\widetilde{v''h''h''}\right)}_{VI_y}+\underbrace{\overline{h''}\left(-\frac{\partial\overline{q_x^{cd}}}{\partial x}-\frac{\partial\overline{q_y^{cd}}}{\partial y}+\overline{N}\right)}_{VII},
\end{aligned}
\tag{4.14}
$$

where on the right-hand side of (4.14) there are the streamwise and wall-normal mean convective terms (I_x and I_y), the streamwise and wall-normal molecular diffusion (II_x

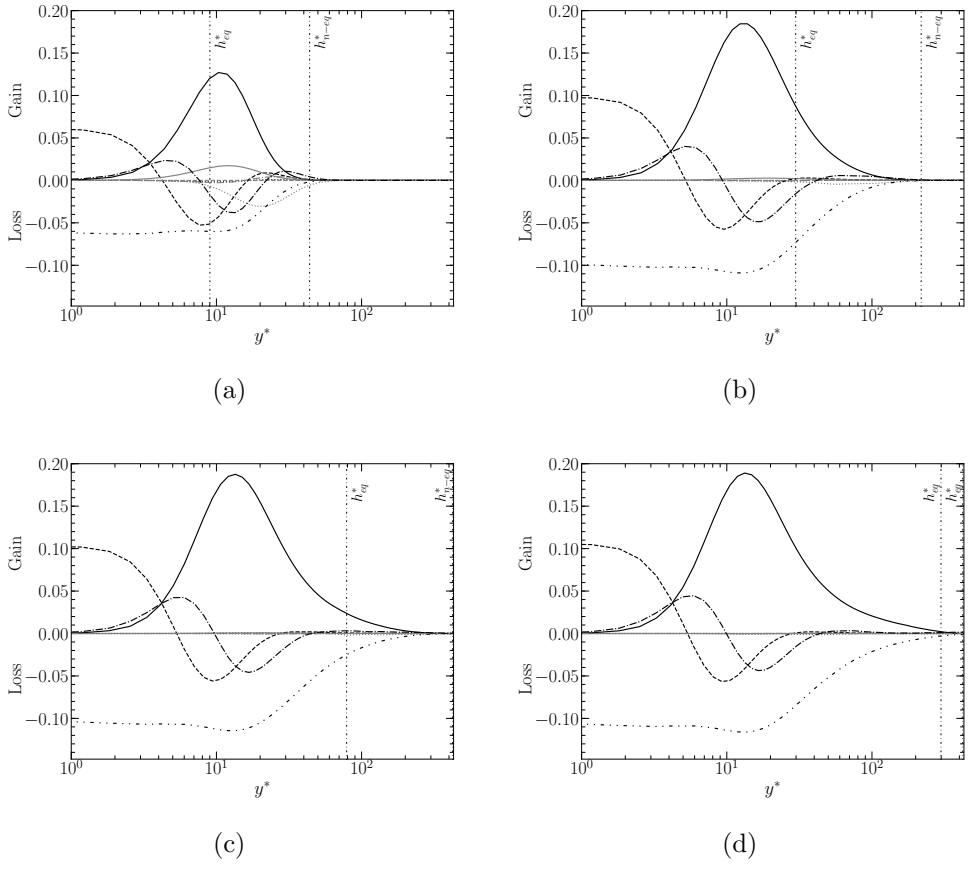

Figure 24: Budgets of enthalpy variance at $x/\delta = 0.73$ (a), 2π (b), 5.7π (c) and 16.5π : —— streamwise (V_x: gray) and wall-normal (V_y: black) production; - · · - · · - molecular dissipation III; - - - - - streamwise (II_x: gray) and wall-normal (II_y: black) molecular diffusion; – · – · – streamwise (VI_x: gray) and wall-normal (VI_y: black) turbulent diffusion; · · · · · · streamwise (I_x: gray) and wall-normal (I_y: black) mean convective terms.

and II_y), molecular dissipation (III), a term of correlation between enthalpy and N (IV) where $N = \frac{\mathrm{D}p}{\mathrm{D}t} + \boldsymbol{\tau}_{ij}\frac{\partial u_i}{\partial x_j} + S_{ener}$ regroups the compressibility effects and the source term (see appendix A), the streamwise and wall-normal production terms (V_x and V_y), the streamwise and wall-normal turbulent diffusion terms (VI_x and VI_y) and a term related to the enthalpy-density correlation (VII).

Figure 24 shows the evolution of the different terms (scaled with respect to $\overline{q_w}(x)^2/\overline{\mu_w}(x)$) for different crosswise sections. For each subplot at a given x/δ, the respective h^*_{eq} and h^*_{n-eq} defined in section §4.3 are put into evidence. Some terms (IV and VII), being always small and negligible, are not plotted.

Figure 24a is relative to $x/\delta = 0.73$. At this close distance from the leading edge, the different terms of (4.14) are active only in a small portion (approximately 10%) of the boundary layer which is delimited by h^*_{n-eq}, beyond which the flow is still not affected by the heated wall. It is between h^*_{eq} and h^*_{n-eq} that the non-equilibrium effects can be observed. The classic contributions (wall-normal production, molecular dissipation and wall-normal turbulent and molecular diffusion) are far from being fully developed and

the streamwise convective and production terms are not negligible. On the other hand, even at this close distance from the leading edge, the wall-normal convective term as well as the streamwise molecular and turbulent diffusion can be neglected.
Figure 24b is relative to $x/\delta = 2\pi$. It is interesting to notice how at this crosswise section all the non-equilibrium terms in the temperature variance budget (even the streamwise production and the streamwise convective term) have disappeared. In the region between h^*_{eq} and h^*_{n-eq}, while the mean energy balance presents strong streamwise non-equilibrium terms as seen in §4.3, the enthalpy variance budget seems to merely feature the gradual development of the classic budget terms. For $y^* < h^*_{eq}$, which represents the equilibrium region where the mean energy balance is equilibrated and the temperature profile is very close to the equilibrium, the different contributions controlling the r.m.s. temperature have also settled as it can be seen in figures 24b, 24c and 24d. Comparing these figures one can observe, for example, that the peak of production or the level of wall-normal molecular diffusion at the wall are identical.

Concerning the wall-normal turbulent heat flux, the time-averaged transport equation reads (see A.2 for the details):

$$
\begin{aligned}
0 = &\underbrace{-\frac{\partial}{\partial x}\left(\overline{\rho}\widetilde{u}\widetilde{v''h''}\right)}_{I_x}\underbrace{-\frac{\partial}{\partial y}\left(\overline{\rho}\widetilde{v}\widetilde{v''h''}\right)}_{I_y}+\underbrace{\frac{\partial}{\partial x}\left(\overline{\tau'_{2,1}h'}-\overline{q_x^{cd'}u'}\right)}_{II_x}+\underbrace{\frac{\partial}{\partial y}\left(\overline{\tau'_{2,2}h'}-\overline{q_y^{cd'}v'}\right)}_{II_y}+\\
&\underbrace{-\left(\overline{\tau'_{2,1}\frac{\partial h'}{\partial x}}+\overline{\tau'_{2,2}\frac{\partial h'}{\partial y}}+\overline{\tau'_{2,3}\frac{\partial h'}{\partial z}}\right)+\left(\overline{q_x^{cd'}\frac{\partial v'}{\partial x}}+\overline{q_y^{cd'}\frac{\partial v'}{\partial y}}+\overline{q_z^{cd'}\frac{\partial v'}{\partial z}}\right)}_{III}\underbrace{-\overline{h'\frac{\partial p'}{\partial y}}}_{IV}+\underbrace{\overline{v'N'}}_{V}+\\
&\underbrace{-\overline{\rho}\widetilde{u''h''}\frac{\partial\widetilde{v}}{\partial x}-\overline{\rho}\widetilde{u''v''}\frac{\partial\widetilde{h}}{\partial x}}_{VI_x}\underbrace{-\overline{\rho}\widetilde{v''h''}\frac{\partial\widetilde{v}}{\partial y}-\overline{\rho}\widetilde{v''v''}\frac{\partial\widetilde{h}}{\partial y}}_{VI_y}\underbrace{-\frac{\partial}{\partial x}\left(\overline{\rho}\widetilde{u''v''h''}\right)}_{VII_x}\underbrace{-\frac{\partial}{\partial y}\left(\overline{\rho}\widetilde{v''v''h''}\right)}_{VII_y}+\\
&\underbrace{+\overline{h''}\left(-\frac{\partial\overline{p}}{\partial y}+\frac{\partial\overline{\tau_{2,1}}}{\partial x}+\frac{\partial\overline{\tau_{2,2}}}{\partial y}\right)+\overline{v''}\left(\overline{N}-\frac{\partial\overline{q_x^{cd'}}}{\partial x}-\frac{\partial\overline{q_y^{cd'}}}{\partial y}\right)}_{VIII},
\end{aligned}
\tag{4.15}
$$

where on the right-hand side of the equation there are the mean streamwise and wall-normal convective terms (I_x and I_y), the streamwise and wall-normal molecular diffusion (II_x and II_y), the molecular dissipation (III), the enthalpy-pressure-gradient correlation (IV), the correlation between the wall-normal velocity and N (V) where N regroups the compressibility effects and the source term (see appendix A), the streamwise and wall-normal production (VI_x and VI_y), the streamwise and wall-normal turbulent diffusion (VII_x and VII_y) and two terms related to the enthalpy-density and wall-normal-velocity-density correlations ($VIII$).
Figure 25 shows the evolution of the different terms (scaled with respect to $\overline{q_w}(x)\overline{\tau_w}(x)/\overline{\mu_w}(x)$) for different crosswise sections with the respective h^*_{eq} and h^*_{n-eq} defined in section §4.3. The terms V and $VIII$ are always small and negligible and are not plotted.
Most of the observations made concerning the budgets of enthalpy variance are still valid. The non-equilibrium region $h^*_{eq} < y^* < h^*_{n-eq}$ manifests with a gradual development of the classic terms (including, in this case, the enthalpy-pressure-gradient) rather than with the presence of strong streamwise terms as seen in section §4.3 for the mean energy balance. Concerning the wall-normal turbulent heat flux budgets, the only streamwise terms that are important near the leading edge are the streamwise production and

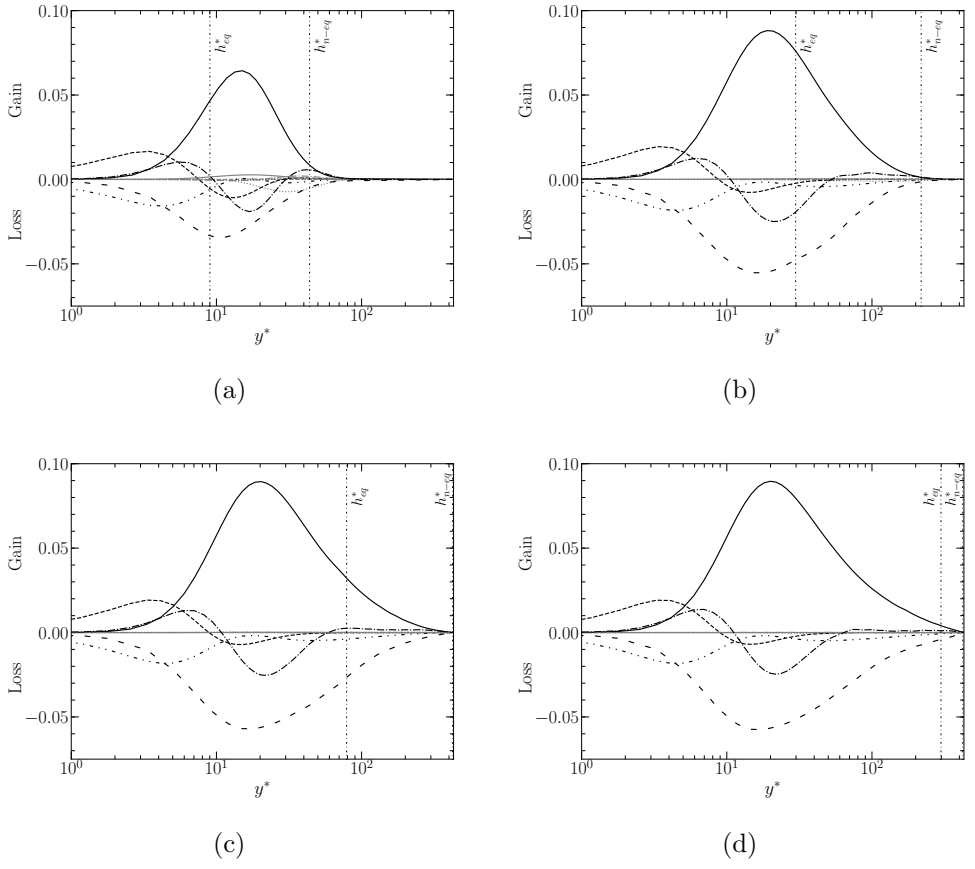

Figure 25: Budgets of wall-normal turbulent heat flux at $x/\delta = 0.73$ (a), 2π (b), 5.7π (c) and 16.5π: —— streamwise (VI_x: gray) and wall-normal (VI_y: black) production; - · · · · · - molecular dissipation III; - - - - - streamwise (II_x: gray) and wall-normal (II_y: black) molecular diffusion; – · – · – streamwise (VII_x: gray) and wall-normal (VII_y: black) turbulent diffusion; ····· streamwise (I_x: gray) and wall-normal (I_y: black) convective terms; - - - - - enthalpy-pressure-gradient correlation IV.

convection, as shown in figure 25a. Yet, even these terms become negligible at $x/\delta = 2\pi$ (see Fig. 25b).

It is evident that also in this budget, the definitions of h^*_{eq} and h^*_{n-eq} are suited for describing the evolution towards equilibrium of the different terms of 4.15. For every x/δ, between the wall and h^*_{eq} the classic budgets have settled while between h^*_{n-eq} and the centre of the channel all the terms are essentially zero. Figure 26 shows the details of the budgets of enthalpy variance and wall-normal turbulent heat flux for $y^* \sim h^*_{n-eq}$ at $x/\delta = 0.73$, *i.e.*, the same crosswise section of figures 24a and 25a. In both figures 26a and 26b, it can be seen how, at this distance from the leading edge, the turbulent diffusion plays an important role in the development of both enthalpy fluctuations and enthalpy-wall-normal velocity correlation. In the case of the enthalpy variance (see Fig. 26a), turbulent diffusion is actually the only term inducing a gain of enthalpy fluctuations, mostly counterbalanced by the mean streamwise convective term. The presence of non-negligible turbulent diffusion around $y^* \sim h^*_{n-eq}$ corroborates the hypothesis formulated in §4.3, *i.e.*, that the fast decay of the temperature-homogeneous

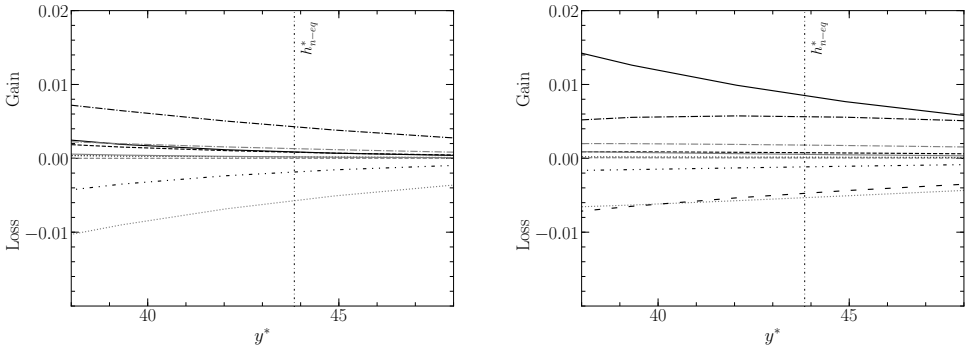

Figure 26: Budgets of enthalpy variance (a) and wall-normal turbulent heat flux (b) at $x/\delta = 0.73$ zoomed at $y^* \sim h^*_{n-eq}$. See figures 24 and 25 for the notation.

region beyond $y^* > h^*_{n-eq}$ might be due to the efficient heat transport carried out by turbulence.

4.5. *Turbulent Prandtl number*

When heat transfer is considered in turbulence modelling (either RANS or LES), the turbulent transport in the mean energy balance is commonly modelled via the definition of a turbulent eddy conductivity λ_t, which plays the same role of the turbulent eddy viscosity ν_t in the momentum equation. A simple way of relating λ_t and ν_t is based on the definition of a turbulent Prandtl number, analogous to the molecular Prandtl number and thus defined as

$$\mathrm{Pr}_t = \frac{\overline{\rho}\nu_t\overline{c_p}}{\lambda_t} = \frac{-\overline{\rho}\widetilde{u''v''}}{-\overline{\rho}\widetilde{v''h''}/\overline{c_p}}\frac{\mathrm{d}\overline{T}/\mathrm{d}y}{\mathrm{d}\overline{u}/\mathrm{d}y} \ . \tag{4.16}$$

Its relevance in complex three-dimensional turbulent flows is arguable but because of its applicability in simpler flows such as thin shear layers, a great number of analytical, numerical and experimental investigations have been carried out (see Kays 1994). Blom (1970) analysed the evolution of the turbulent Prandtl number in a developing thermal boundary layer and found out that it varies in both wall-normal and streamwise directions while suggesting that a universal distribution of Pr_t can only be expected in the near-wall region. Antonia *et al.* (1977) carried out similar investigations and found that the turbulent Prandtl number is generally in the order of magnitude of one, thus showing the overall validity of the Reynolds analogy; according to their experimental results, values of Pr_t strongly exceeding unity can only be found in the proximity of the leading edge of the thermal boundary layer.

Given the difficulty of experimentally measuring the turbulent Prandtl number, direct numerical simulation, despite being strongly limited in terms of Reynolds number, is a powerful tool for precisely calculating its evolution in boundary layers and improve current turbulence models, even in modern simulations. Indeed, the turbulent Prandtl number is extensively used in wall-modelled large-eddy simulations (see Benarafa *et al.* 2007; Bocquet *et al.* 2012; Zhang *et al.* 2013) and several algebraic models describing its evolution in the wall-normal direction have been proposed (see Kays 1994; Weigand *et al.* 1997).

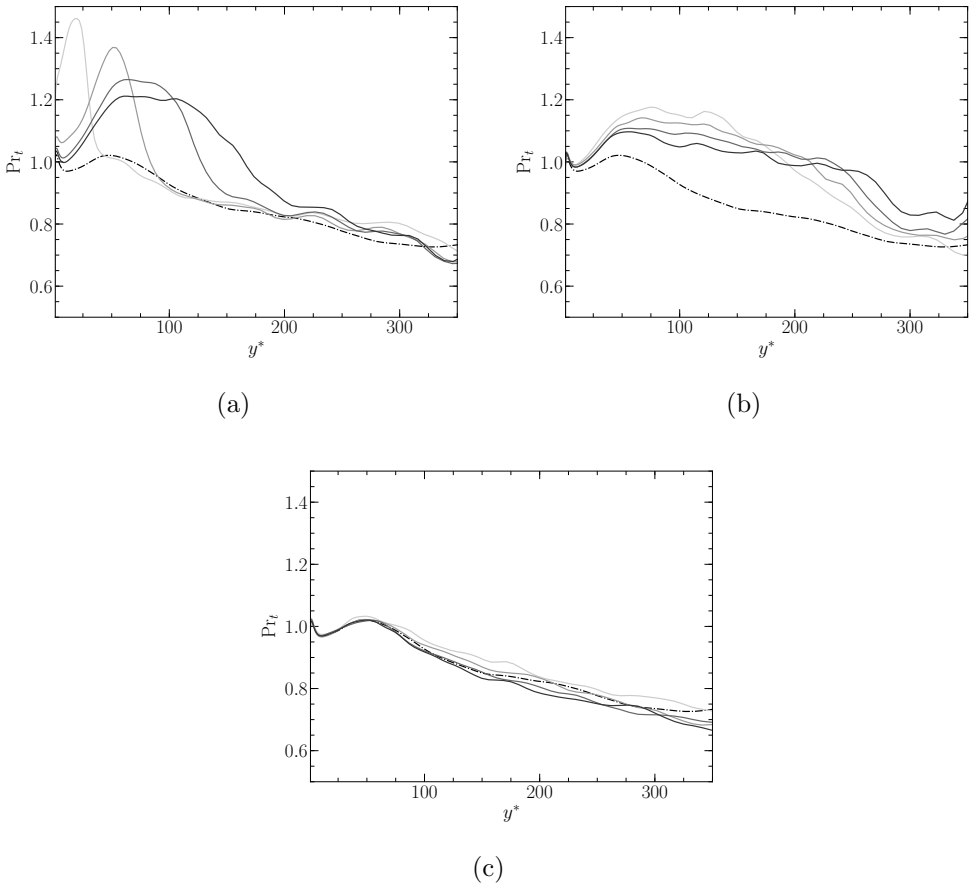

Figure 27: Evolution of turbulent Prandtl number in the wall-normal direction for different x/δ: —— present results at (from light to dark gray) $x/\delta = 0.18$, 0.73 0.5π and 0.75π (a), at $x/\delta = \pi$, 1.25π, 1.5π and 1.75π (b); at $x/\delta = 5.67\pi$, 8.25π, 10.8π and 16.5π (c); – · – · – profile of equilibrium configuration of section §3.2.

Figure 27 shows the evolution of the turbulent Prandtl number in the wall-normal direction for different x/δ compared to the profile of the equilibrium configuration described in section §3.2.

The dashed-dotted line represents the equilibrium profile: it can be seen that Pr_t is slightly greater than unity at the wall before decreasing and attaining $\mathrm{Pr}_t \approx 0.7$ in the channel core flow. Its mild gradient along the wall-normal direction can justify the use of a constant average turbulent Prandtl number (usually $\mathrm{Pr}_t \approx 0.9$) in both wall-modeled and wall-resolved LES, at least in equilibrium boundary layers (see Kawai & Larsson 2012; Fu *et al.* 2018).

Figure 27a shows the evolution of Pr_t for four crosswise sections which are relatively close to the leading edge. As can be seen, the turbulent Prandtl number is larger compared to equilibrium, even in the near-wall region where the thermal boundary layer is supposed to be at equilibrium. Similarly to the temperature root-mean-square profiles, the settlement of the turbulent Prandtl number is longer than the mean temperature. As x/δ increases, the turbulent Prandtl number profiles decrease until converging towards its value at equilibrium; besides that, the peak shifts towards the higher y^* while its value decreases.

The same tendency can be observed in figure 27b for x/δ ranging between $[\pi, 1.75\pi]$ while in figure 27c it is shown how the turbulent Prandtl number essentially returns to equilibrium for $x/\delta \gtrsim 5\pi$. The peak larger values of Pr_t are explained from the ratio between the turbulent eddy viscosity and conductivity. The numerator, ν_t, is already well-established with the incoming adiabatic turbulent boundary layer. On the other hand, λ_t, which quantifies turbulent heat transfer, is initially small and grows as the thermal boundary layers develops.

These results show how the perturbation of the heated wall on the turbulent Prandtl number essentially consists in a limited portion of the boundary layer where Pr_t is higher than at equilibrium and, in particular, exceeds unity; the effect is, as expected, more important in proximity of the leading edge; the results are therefore in qualitative agreement with those of Antonia *et al.* (1977). Despite the perturbation of the turbulent Prandtl number, its value remains in the order of magnitude of one and the Reynolds analogy seems to stand reasonable. Consequently, keeping standard modelling approaches for Pr_t even in the case of a developing boundary layer seems appropriate.
On the other hand, there is no evidence of the existence of a universal distribution in the near-wall region as indicated in Blom (1970). It appears to be quite the opposite since the highest values of Pr_t can be found near the leading edge in the very proximity of the wall.

5. Conclusion

The direct numerical simulation of a thermal turbulent boundary layer developing in a channel flow is performed. The flow evolves from a fully turbulent adiabatic, temperature-homogeneous state towards a new equilibrium state characterised by a fully developed thermal boundary layer.

In section §4.2 the impact on the velocity boundary layer is analysed. It is shown that near the leading edge (both downstream and upstream) the streamwise velocity profile deviates from the canonical equilibrium profiles as well as a considerable increase of the wall-normal velocity is observed. The impact of the isothermal wall especially manifests itself through a local perturbation of the wall shear stress and, consequently, of the streamwise pressure gradient. A wall scaling taking into account the mean fluid property variations as well as the streamwise pressure gradient (which slightly differs from the one proposed by Manhart *et al.* (2008)) is therefore introduced, allowing to make the mean streamwise velocity and all the r.m.s. velocity profiles collapse on the equilibrium ones. Due to the small temperature ratio between the wall and the centre of the channel, the perturbation is small and localised in a very limited portion of the channel flow. The solution proposed is thus to be considered appropriate, *a priori*, only in this particular context.

The evolution of the mean temperature is described in section §4.3. It is shown that for every crosswise section there is always a part of the boundary layer, which can be very small near the leading edge, where the thermal boundary layer can be considered at equilibrium. The existence of such an equilibrium layer is an important assumption which may *a priori* justify the use of an equilibrium wall-model in WMLES even when applied to non-equilibrium configurations as long as the modelled portion of the flow lays within the aforesaid equilibrium layer. So as to quantitatively determine the evolution of the equilibrium layer along the channel flow, a criterion based on the different equilibrium and non-equilibrium terms of the mean energy equation is introduced; the equilibrium layer is thus defined as the portion of the boundary layer where the non-equilibrium terms are a negligible contribution to the total heat flux.

The evolution of the r.m.s. temperature as well as the wall-normal turbulent heat flux is shown in section §4.4. The respective transport equations are also analysed; it is shown how the mean streamwise contributions are always small, even in the early development stage of the thermal boundary layer; it is also shown how within the equilibrium layer all the different budgets are fully developed.

Finally, the evolution of the turbulent Prandtl number is described in section §4.5. It is shown how, despite always staying within the same order of magnitude, the turbulent Prandtl number is impacted and exceeds unity in a relatively large portion of the developing boundary layer; it is also shown how there is no evidence of a universal behaviour of the turbulent Prandtl number in the near-wall region.

Results are obtained for a unique flow regime in terms of temperature ratio and Reynolds number. Therefore, other flow regimes need to be studied in order to generalise these results for the sake of RANS or LES modelling of turbulent heat transfer.

Acknowledgements

The numerical study was carried out thanks to the HPC resources of TTGC under the allocation 2018-A0042B10159 made by GENCI, and the HPC resources from the "Mésocentre" computing centre of Centrale- Supélec and École Normale Supérieure Paris-Saclay supported by CNRS and grants from Ministry of Research via the Contrat Plan État-Région.

Declaration of interests

The authors report no conflict of interest.

Appendix A. Derivation of averaged enthalpy variance and wall-normal turbulent heat flux transport equations

A.1. *Averaged transport equation for the enthalpy variance*

The energy balance reads (see (2.3)):

$$\frac{\partial \rho h}{\partial t} + \frac{\partial \rho u_j h}{\partial x_j} = \frac{\mathrm{D}p}{\mathrm{D}t} - \frac{\partial q_j^{cd}}{\partial x_j} + \boldsymbol{\tau}_{ij}\frac{\partial u_i}{\partial x_j} + S_{ener} \ , \tag{A 1}$$

which can also be rewritten as:

$$\frac{\partial \rho h}{\partial t} + \frac{\partial \rho u_j h}{\partial x_j} = -\frac{\partial q_j^{cd}}{\partial x_j} + N \ , \tag{A 2}$$

where N regroups all those terms (pressure material derivative, viscous dissipation and source term) which play a marginal role in the derivation of the transport equation. Applying the Reynolds average to (A 2), one has:

$$\frac{\partial}{\partial t}\overline{\rho}\widetilde{h} + \frac{\partial}{\partial x_j}\overline{\rho}\widetilde{u_j}\widetilde{h} = -\frac{\partial \overline{q_j^{cd}}}{\partial x_j} - \frac{\partial}{\partial x_j}\overline{\rho}\widetilde{u_j''h''} + \overline{N} \ , \tag{A 3}$$

which, multiplied by $\widetilde{h}$, gives:

$$\frac{\partial}{\partial t}\overline{\rho}\frac{\widetilde{h}^2}{2} + \frac{\partial}{\partial x_j}\overline{\rho}\widetilde{u_j}\frac{\widetilde{h}^2}{2} = -\widetilde{h}\frac{\partial \overline{q_j^{cd}}}{\partial x_j} - \widetilde{h}\frac{\partial}{\partial x_j}\overline{\rho}\widetilde{u_j''h''} + \widetilde{h}\overline{N} \ . \tag{A 4}$$

On the other hand, multiplying (A 2) by h and applying the Reynolds average, one has:

$$\frac{\partial}{\partial t}\overline{\rho}\frac{\widetilde{h^2}}{2}+\frac{\partial}{\partial x_j}\overline{\rho}\frac{\widetilde{u_j h^2}}{2}=-\overline{h\frac{\partial q_j^{cd}}{\partial x_j}}+\overline{hN}\ , \tag{A 5}$$

allowing to obtain the transport equation for $\widetilde{h''^2}=\widetilde{h^2}-\widetilde{h}^2$ by simply subtracting (A 4) from (A 5):

$$\frac{\partial}{\partial t}\overline{\rho}\frac{\widetilde{h''^2}}{2}+\frac{\partial}{\partial x_j}\left[\overline{\rho}\frac{\widetilde{u_j h^2}}{2}-\overline{\rho}\widetilde{u_j}\frac{\widetilde{h}^2}{2}\right]=-\overline{h\frac{\partial q_j^{cd}}{\partial x_j}}+\widetilde{h}\frac{\partial\overline{q_j^{cd}}}{\partial x_j}+\widetilde{h}\frac{\partial}{\partial x_j}\overline{\rho}\widetilde{u_j''h''}+\overline{hN}-\widetilde{h}\overline{N}\ . \tag{A 6}$$

After several developments and simplifications, (A 6) can be rewritten as:

$$\begin{aligned}\frac{\partial}{\partial t}\overline{\rho}\frac{\widetilde{h''^2}}{2}+\frac{\partial}{\partial x_j}\overline{\rho}\frac{\widetilde{u_j}\widetilde{h''^2}}{2}=&-\frac{\partial}{\partial x_j}\overline{q_j^{cd'}h'}+\overline{q_j^{cd'}\frac{\partial h'}{\partial x_j}}+\overline{h'N'}-\overline{\rho}\widetilde{u_j''h''}\frac{\partial\widetilde{h}}{\partial x_j}+\\&-\frac{1}{2}\frac{\partial}{\partial x_j}\overline{\rho}\widetilde{u_j''h''h''}+\overline{h''}\left(-\frac{\partial\overline{q_j^{cd}}}{\partial x_j}+\overline{N}\right)\ ,\end{aligned} \tag{A 7}$$

where $\overline{h''}$ can also be written as $-\overline{\rho'h'}/\overline{\rho}$.
The unsteady term as well as all derivatives of mean quantities in the spanwise direction are zero, which leads to the final expression of the mean transport equation for the enthalpy variance:

$$\begin{aligned}0=&\underbrace{-\frac{\partial}{\partial x}\left(\overline{\rho}\widetilde{u}\frac{\widetilde{h''^2}}{2}\right)}_{I_x}\underbrace{-\frac{\partial}{\partial y}\left(\overline{\rho}\widetilde{v}\frac{\widetilde{h''^2}}{2}\right)}_{I_y}\underbrace{-\frac{\partial}{\partial x}\left(\overline{q_x^{cd'}h'}\right)}_{II_x}\underbrace{-\frac{\partial}{\partial y}\left(\overline{q_y^{cd'}h'}\right)}_{II_y}+\\&+\underbrace{\overline{q_x^{cd'}\frac{\partial h'}{\partial x}}+\overline{q_y^{cd'}\frac{\partial h'}{\partial y}}+\overline{q_z^{cd'}\frac{\partial h'}{\partial z}}}_{III}+\underbrace{\overline{h'N'}}_{IV}\underbrace{-\overline{\rho}\widetilde{u''h''}\frac{\partial\widetilde{h}}{\partial x}}_{V_x}\underbrace{-\overline{\rho}\widetilde{v''h''}\frac{\partial\widetilde{h}}{\partial y}}_{V_y}+\\&\underbrace{-\frac{1}{2}\frac{\partial}{\partial x}\left(\overline{\rho}\widetilde{u''h''h''}\right)}_{VI_x}\underbrace{-\frac{1}{2}\frac{\partial}{\partial y}\left(\overline{\rho}\widetilde{v''h''h''}\right)}_{VI_y}+\underbrace{\overline{h''}\left(-\frac{\partial\overline{q_x^{cd}}}{x}-\frac{\partial\overline{q_y^{cd}}}{y}+\overline{N}\right)}_{VII}\ ,\end{aligned} \tag{A 8}$$

where on the right-hand side of (A 8) there are the mean streamwise and wall-normal convective terms (I_x and I_y), the streamwise and wall-normal molecular diffusion (II_x and II_y), molecular dissipation (III), a term of correlation between enthalpy and N (IV) where N regroups the compressibility effects and the source term, the streamwise and wall-normal production terms (V_x and V_y), the streamwise and wall-normal turbulent diffusion terms (VI_x and VI_y) and a term related to the enthalpy-density correlation (VII).

A.2. *Averaged transport equation for the wall-normal turbulent heat flux*

In order to obtain the transport equation for $\widetilde{v''h''}$, both the energy equation (2.3) and the momentum equation (2.2) projected along the wall-normal direction are needed. The latter reads:

$$\frac{\partial\rho v}{\partial t}+\frac{\partial\rho v u_j}{\partial x_j}=-\frac{\partial p}{\partial y}+\frac{\partial\boldsymbol{\tau}_{2j}}{\partial x_j}\ , \tag{A 9}$$

which, once the Reynolds average is applied, gives:

$$\frac{\partial}{\partial t}\overline{\rho}\widetilde{v}+\frac{\partial}{\partial x_j}\overline{\rho}\widetilde{v}\widetilde{u_j}=-\frac{\partial\overline{p}}{\partial y}+\frac{\partial\overline{\boldsymbol{\tau}_{2j}}}{\partial x_j}-\frac{\partial}{\partial x_j}\overline{\rho}\widetilde{u_j''v''}\ . \tag{A 10}$$

Now, by multiplying (A 10) by $\widetilde{h}$ and the averaged energy equation (A 3) by $\widetilde{v}$ and summing them, one has:

$$\frac{\partial}{\partial t}\overline{\rho}\widetilde{v}\widetilde{h}+\frac{\partial}{\partial x_j}\overline{\rho}\widetilde{u_j}\widetilde{v}\widetilde{h}=-\widetilde{h}\frac{\partial\overline{p}}{\partial y}+\widetilde{h}\frac{\partial\overline{\boldsymbol{\tau}_{2j}}}{\partial x_j}-\widetilde{v}\frac{\partial\overline{q_j^{cd}}}{\partial x_j}+\widetilde{v}\overline{N}-\widetilde{h}\frac{\partial}{\partial x_j}\overline{\rho}\widetilde{u_j''v''}-\widetilde{v}\frac{\partial}{\partial x_j}\overline{\rho}\widetilde{u_j''h''}\ , \tag{A 11}$$

which is a transport equation for $\widetilde{v}\widetilde{h}$. A similar equation for $\widetilde{vh}$ can be obtained by multiplying ((A 9)) by h, ((A 2)) by v and averaging the sum:

$$\begin{aligned}\frac{\partial}{\partial t}\overline{\rho}\widetilde{vh}+\frac{\partial}{\partial x_j}\overline{\rho}u_j\widetilde{vh}=&-\overline{h\frac{\partial p}{\partial y}}+\overline{h\frac{\partial\boldsymbol{\tau}_{2j}}{\partial x_j}}-\overline{v\frac{\partial q_j^{cd}}{\partial x_j}}+\overline{vN}+\\&-\frac{\partial}{\partial x_j}\overline{\rho}\widetilde{u_j''v''h''}-\frac{\partial}{\partial x_j}\overline{\rho}\widetilde{h}\widetilde{u_j''v''}-\frac{\partial}{\partial x_j}\overline{\rho}\widetilde{v}\widetilde{u_j''h''}\ .\end{aligned} \tag{A 12}$$

The transport equation for $\widetilde{v''h''}$ is obtained subtracting (A 11) to (A 12), which, after several developments and simplifications, gives:

$$\begin{aligned}\frac{\partial}{\partial t}\overline{\rho}\widetilde{v''h''}+\frac{\partial}{\partial x_j}\overline{\rho}\widetilde{u_j}\widetilde{v''h''}=&\frac{\partial}{\partial x_j}\overline{\boldsymbol{\tau}'_{2j}h'}-\frac{\partial}{\partial x_j}\overline{q_j^{cd'}v'}-\overline{\boldsymbol{\tau}'_{2j}\frac{\partial h'}{\partial x_j}}+\overline{q_j^{cd'}\frac{\partial v'}{\partial x_j}}+\\&-\overline{h'\frac{\partial p'}{\partial y}}+\overline{v'N'}-\overline{\rho}\widetilde{u_j''v''}\frac{\partial\widetilde{h}}{\partial x_j}-\overline{\rho}\widetilde{u_j''h''}\frac{\partial\widetilde{v}}{\partial x_j}+\\&-\frac{\partial}{\partial x_j}\overline{\rho}\widetilde{u_j''v''h''}+\overline{h''}\left(-\frac{\partial\overline{p}}{\partial y}+\frac{\partial\overline{\boldsymbol{\tau}_{2j}}}{\partial x_j}\right)+\\&+\overline{v''}\left(\overline{N}-\frac{\partial\overline{q_j^{cd}}}{\partial x_j}\right)\ ,\end{aligned} \tag{A 13}$$

where $\overline{v''}=-\overline{\rho'v'}/\overline{\rho}$ and $\overline{h''}=-\overline{\rho'h'}/\overline{\rho}$.
Finally, the unsteady term as well as all derivatives of mean quantities along the spanwise direction are zero, giving the final expression of the averaged transport equation of the wall-normal turbulent heat flux:

$$\begin{aligned}0=&\underbrace{-\frac{\partial}{\partial x}\left(\overline{\rho}\widetilde{u}\widetilde{v''h''}\right)}_{I_x}\underbrace{-\frac{\partial}{\partial y}\left(\overline{\rho}\widetilde{v}\widetilde{v''h''}\right)}_{I_y}+\underbrace{\frac{\partial}{\partial x}\left(\overline{\tau'_{2,1}h'}-\overline{q_x^{cd'}u'}\right)}_{II_x}+\underbrace{\frac{\partial}{\partial y}\left(\overline{\tau'_{2,2}h'}-\overline{q_y^{cd'}v'}\right)}_{II_y}+\\&\underbrace{-\left(\overline{\tau'_{2,1}\frac{\partial h'}{\partial x}}+\overline{\tau'_{2,2}\frac{\partial h'}{\partial y}}+\overline{\tau'_{2,3}\frac{\partial h'}{\partial z}}\right)+\left(\overline{q_x^{cd'}\frac{\partial v'}{\partial x}}+\overline{q_y^{cd'}\frac{\partial v'}{\partial y}}+\overline{q_z^{cd'}\frac{\partial v'}{\partial z}}\right)}_{III}\underbrace{-\overline{h'\frac{\partial p'}{\partial y}}}_{IV}+\underbrace{\overline{v'N'}}_{V}+\\&\underbrace{-\overline{\rho}\widetilde{u''h''}\frac{\partial\widetilde{v}}{\partial x}-\overline{\rho}\widetilde{u''v''}\frac{\partial\widetilde{h}}{\partial x}}_{VI_x}\underbrace{-\overline{\rho}\widetilde{v''h''}\frac{\partial\widetilde{v}}{\partial y}-\overline{\rho}\widetilde{v''v''}\frac{\partial\widetilde{h}}{\partial y}}_{VI_y}\underbrace{-\frac{\partial}{\partial x}\left(\overline{\rho}\widetilde{u''v''h''}\right)}_{VII_x}\underbrace{-\frac{\partial}{\partial y}\left(\overline{\rho}\widetilde{v''v''h''}\right)}_{VII_y}+\\&\underbrace{+\overline{h''}\left(-\frac{\partial\overline{p}}{\partial y}+\frac{\partial\overline{\tau_{2,1}}}{\partial x}+\frac{\partial\overline{\tau_{2,2}}}{\partial y}\right)+\overline{v''}\left(\overline{N}-\frac{\partial\overline{q_x^{cd'}}}{\partial x}-\frac{\partial\overline{q_y^{cd'}}}{\partial y}\right)}_{VIII}\ ,\end{aligned} \tag{A 14}$$

where on the right-hand side of the equation there are the mean streamwise and wall-normal convective terms (I_x and I_y), the streamwise and wall-normal molecular diffusion (II_x and II_y), the molecular dissipation (III), the enthalpy-pressure-gradient correlation (IV), the correlation between the wall-normal velocity and N (V) where N regroups the compressibility effects and the source term (see §A.1), the streamwise and wall-normal production (VI_x and VI_y), the streamwise and wall-normal turbulent diffusion (VII_x and VII_y) and two terms related to the enthalpy-density and wall-normal-velocity-density correlations ($VIII$).

REFERENCES

Abe, Hiroyuki, Kawamura, Hiroshi & Matsuo, Yuichi 2001 Direct numerical simulation of a fully developed turbulent channel flow with respect to the reynolds number dependence. *J. Fluids Eng.* **123** (2), 382–393.

Antonia, RA, Danh, HQ & Prabhu, A 1977 Response of a turbulent boundary layer to a step change in surface heat flux. *Journal of Fluid Mechanics* **80** (1), 153–177.

Bellec, Morgane, Toutant, Adrien & Olalde, Gabriel 2017 Large eddy simulations of thermal boundary layer developments in a turbulent channel flow under asymmetrical heating. *Computers & Fluids* **151**, 159–176.

Benarafa, Y, Cioni, O, Ducros, F & Sagaut, P 2007 Temperature wall modelling for large-eddy simulation in a heated turbulent plane channel flow. *International journal of heat and mass transfer* **50** (21-22), 4360–4370.

Biles, Drummond, Ebadi, Alireza, Allard, Michael P & White, Christopher M 2019 The design and validation of a thermal boundary layer wall plate. *Journal of Fluids Engineering* **141** (12).

Blom, J 1970 Experimental determination of the turbulent prandtl number in a developing temperature boundary layer. 4th int. In *Heat Transfer Conf., Paris—Versailles*, , vol. 2.

Bocquet, S, Sagaut, P & Jouhaud, J 2012 A compressible wall model for large-eddy simulation with application to prediction of aerothermal quantities. *Physics of fluids* **24** (6), 065103.

Coleman, Gary N, Kim, John & Moser, Robert D 1995 A numerical study of turbulent supersonic isothermal-wall channel flow. *Journal of Fluid Mechanics* **305**, 159–183.

Colin, Olivier & Rudgyard, Michael 2000 Development of high-order taylor–galerkin schemes for les. *Journal of Computational Physics* **162** (2), 338–371.

Eames, I & Hunt, JCR 1997 Inviscid flow around bodies moving in weak density gradients without buoyancy effects. *Journal of Fluid Mechanics* **353**, 331–355.

Fu, Lin, Karp, M, Bose, ST, Moin, P & Urzay, J 2018 Equilibrium wall-modeled les of shock-induced aerodynamic heating in hypersonic boundary layers. *Bulletin of the American Physical Society* **63**.

Fulachier, Louis 1972 Contribution à l'étude des analogies des champs dynamique et thermique dans une couche limite turbulente: effet de l'aspiration. PhD thesis, Université de Provence.

Hattori, Hirofumi, Houra, Tomoya & Nagano, Yasutaka 2007 Direct numerical simulation of stable and unstable turbulent thermal boundary layers. *International Journal of Heat and Fluid Flow* **28** (6), 1262–1271.

Hattori, Hirofumi, Yamada, Syohei & Houra, Tomoya 2012 Dns study of effects of suddenly-vanishing wall heating in turbulent boundary layer. *Journal of Thermal Science and Technology* **7** (1), 313–321.

Hattori, Hirofumi, Yamada, Shohei, Tanaka, Masahiro, Houra, Tomoya & Nagano, Yasutaka 2013 Dns, les and rans of turbulent heat transfer in boundary layer with suddenly changing wall thermal conditions. *International journal of heat and fluid flow* **41**, 34–44.

Hoffmann, PH & Perry, AE 1979 The development of turbulent thermal layers on flat plates. *International Journal of Heat and Mass Transfer* **22** (1), 39–46.

Huang, PG, Coleman, GN & Bradshaw, P 1995 Compressible turbulent channel flows: Dns results and modelling. *Journal of Fluid Mechanics* **305**, 185–218.

Huang, PG & Coleman, Gary N 1994 Van driest transformation and compressible wall-bounded flows. *AIAA journal* **32** (10), 2110–2113.

Johnson, DS & Whippany, NJ 1957 Velocity, temperature and heat transfer measurements in a turbulent boundary layer downstream of a stepwise discontinuity in wall temperature. *ASME Trans. J. Appl. Mech* **24**, 2–8.

Johnson, DoSog & others 1959 Velocity and temperature fluctuation measurements in a turbulent boundary layer downstream of a stepwise discontinuity in wall temperature. *J. Appl. Mech.* **26**, 325–336.

Kasagi, N, Tomita, Y & Kuroda, A 1992 Direct numerical simulation of passive scalar field in a turbulent channel flow .

Kawai, Soshi & Larsson, Johan 2012 Wall-modeling in large eddy simulation: Length scales, grid resolution, and accuracy. *Physics of Fluids* **24** (1), 015105.

Kawamura, Hiroshi, Abe, Hiroyuki & Matsuo, Yuichi 1999 Dns of turbulent heat transfer in channel flow with respect to reynolds and prandtl number effects. *International Journal of Heat and Fluid Flow* **20** (3), 196–207.

Kawamura, H, Abe, H & Shingai, K 2000 Dns of turbulence and heat transport in a channel flow with different reynolds and prandtl numbers and boundary conditions. *Turbulence, Heat and Mass Transfer* **3**, 15–32.

Kays, Wiliam M 1994 Turbulent prandtl number. where are we? *ASME Transactions Journal of Heat Transfer* **116**, 284–295.

Kim, John & Moin, Parviz 1989 Transport of passive scalars in a turbulent channel flow. In *Turbulent Shear Flows 6*, pp. 85–96. Springer.

Larsson, Johan, Kawai, Soshi, Bodart, Julien & Bermejo-Moreno, Ivan 2016 Large eddy simulation with modeled wall-stress: recent progress and future directions. *Mechanical Engineering Reviews* **3** (1), 15–00418.

Li, Qiang, Schlatter, Philipp, Brandt, Luca & Henningson, Dan S 2009 Dns of a spatially developing turbulent boundary layer with passive scalar transport. *International Journal of Heat and Fluid Flow* **30** (5), 916–929.

Manhart, Michael, Peller, Nikolaus & Brun, Christophe 2008 Near-wall scaling for turbulent boundary layers with adverse pressure gradient. *Theoretical and Computational Fluid Dynamics* **22** (3-4), 243–260.

Morinishi, Youhei, Tamano, Shinji & Nakabayashi, Koichi 2004 Direct numerical simulation of compressible turbulent channel flow between adiabatic and isothermal walls. *Journal of Fluid Mechanics* **502**, 273–308.

Morkovin, Mark V 1962 Effects of compressibility on turbulent flows. *Mécanique de la Turbulence* **367**, 380.

Moureau, V, Lartigue, G, Sommerer, Y, Angelberger, Christian, Colin, O & Poinsot, Thierry 2005 Numerical methods for unsteady compressible multi-component reacting flows on fixed and moving grids. *Journal of Computational Physics* **202** (2), 710–736.

Ng, TT, Talbot, L & Robben, F 1982 The turbulent boundary layer over a flat plate with strong stepwise heating .

Nicoud, FC 1999 Numerical study of a channel flow with variable properties. ctr annual research briefs 1998.

Nicoud, Franck & Bradshaw, Peter 2000 A velocity transformation for heat and mass transfer. *Physics of Fluids* **12** (1), 237–238.

Ockendon, H, Ockendon, JR & Falle, SAEG 2001 The fanno model for turbulent compressible flow. *Journal of Fluid Mechanics* **445**, 187–206.

Papavassiliou, Dimitrios V & Hanratty, Thomas J 1997 Transport of a passive scalar in a turbulent channel flow. *International journal of heat and mass transfer* **40** (6), 1303–1311.

Patel, Ashish, Peeters, Jurriaan WR, Boersma, Bendiks J & Pecnik, Rene 2015 Semi-local scaling and turbulence modulation in variable property turbulent channel flows. *Physics of Fluids* **27** (9), 095101.

Poinsot, Thierry & Veynante, Denis 2005 *Theoretical and numerical combustion*. RT Edwards, Inc.

Sanchez, Marc, Aulery, Frédéric, Toutant, Adrien & Bataille, Françoise 2014 Large eddy simulations of thermal boundary layer spatial development in a turbulent channel flow. *Journal of Fluids Engineering* **136** (6).

Schonfeld, Thilo & Rudgyard, Michael 1999 Steady and unsteady flow simulations using the hybrid flow solver avbp. *AIAA journal* **37** (11), 1378–1385.

Seki, Yohji & Kawamura, Hiroshi 2005 Dns of turbulent heat transfer in a channel flow with streamwisely varying thermal boundary condition. In *TSFP DIGITAL LIBRARY ONLINE*. Begel House Inc.

Simpson, Roger L 1970 Characteristics of turbulent boundary layers at low reynolds numbers with and without transpiration. *Journal of Fluid Mechanics* **42** (4), 769–802.

Simpson, Roger L 1983 A model for the backflow mean velocity profile. *AIAA journal* **21** (1), 142–143.

Spalding, DB 1961 Heat transfer to a turbulent stream from a surface with a step-wise discontinuity in wall temperature. *International Developments in Heat Transfer* pp. 439–446.

Tamano, S & Morinishi, Y 2006 Effect of different thermal wall boundary conditions on compressible turbulent channel flow at m= 1.5. *Journal of Fluid Mechanics* **548**, 361–373.

Taylor, RP, Love, PH, Coleman, HW & Hosni, MH 1990 Heat transfer measurements in incompressible turbulent flat plate boundary layers with step wall temperature boundary conditions. *ASME Transactions Journal of Heat Transfer* **112**, 245–247.

Teitel, M & Antonia, RA 1993 A step change in wall heat flux in a turbulent channel flow. *International journal of heat and mass transfer* **36** (6), 1707–1709.

Toutant, Adrien & Bataille, Francoise 2013 Turbulence statistics in a fully developed channel flow submitted to a high temperature gradient. *International Journal of Thermal Sciences* **74**, 104–118.

Wardana, ING, Ueda, Toshihisa & Mizomoto, M 1994 Effect of strong wall heating on turbulence statistics of a channel flow. *Experiments in fluids* **18** (1-2), 87–94.

Weigand, B, Ferguson, JR & Crawford, ME 1997 An extended kays and crawford turbulent prandtl number model. *International journal of heat and mass transfer* **40** (17), 4191–4196.

Wu, Xiaohua & Moin, Parviz 2010 Transitional and turbulent boundary layer with heat transfer. *Physics of Fluids* **22** (8), 085105.

Zhang, YF & Vicquelin, Ronan 2016 Controlling bulk reynolds number and bulk temperature in channel flow simulations. *Journal of Computational Physics* **305**, 208–216.

Zhang, YF, Vicquelin, Ronan, Gicquel, Olivier & Taine, Jean 2013 A wall model for les accounting for radiation effects. *International Journal of Heat and Mass Transfer* **67**, 712–723.